

Nuclear lamin A/C phosphorylation by loss of androgen receptor leads to cancer-associated fibroblast activation

Received: 25 June 2023

Accepted: 2 September 2024

Published online: 12 September 2024

 Check for updates

Soumitra Ghosh^{1,2,6}✉, Jovan Isma^{2,3}, Paola Ostano⁴, Luigi Mazzeo², Annagiada Toniolo², Monalisa Das², Joni R. White³, Christian Simon^{1,5} & G. Paolo Dotto^{1,2,3,5}✉

Alterations in nuclear structure and function are hallmarks of cancer cells. Little is known about these changes in Cancer-Associated Fibroblasts (CAFs), crucial components of the tumor microenvironment. Loss of the androgen receptor (AR) in human dermal fibroblasts (HDFs), which triggers early steps of CAF activation, leads to nuclear membrane changes and micronuclei formation, independent of cellular senescence. Similar changes occur in established CAFs and are reversed by restoring AR activity. AR associates with nuclear lamin A/C, and its loss causes lamin A/C nucleoplasmic redistribution. AR serves as a bridge between lamin A/C and the protein phosphatase PPP1. Loss of AR decreases lamin-PPP1 association and increases lamin A/C phosphorylation at Ser 301, a characteristic of CAFs. Phosphorylated lamin A/C at Ser 301 binds to the regulatory region of CAF effector genes of the myofibroblast subtype. Expression of a lamin A/C Ser301 phosphomimetic mutant alone can transform normal fibroblasts into tumor-promoting CAFs.

Alterations in nuclear structure and function are characteristic of tumor cells and are often used as prognostic and diagnostic markers^{1–3}. However, the existence and functional significance of nuclear alterations in surrounding stromal cells and, specifically, cancer-associated fibroblasts (CAFs) have yet to be explored. CAFs, a major component of the tumor microenvironment, consist of heterogeneous populations of cells with distinct tumor-enhancing properties^{4–11}.

Senescence of cells, linked to the aging process, can act as a fail-safe mechanism against cancer but also promote it through the production of a battery of pro-tumorigenic cytokines and matrix remodeling enzymes—the Senescence Associated Secretory Phenotype (SASP)^{12,13}. Cumulative evidence from our laboratory indicates that androgen receptor (AR) plays a dual role in skin cancer that is closely intertwined but can be genetically dissociated from that of senescence. In melanoma cells, genetic and pharmacological

inhibition of AR trigger senescence, genomic DNA breakage and suppression of tumorigenesis¹⁴, while increased AR expression makes melanoma cells resistant to targeted therapy (BRAF inhibitors)¹⁵. Countering these intrinsic tumor-promoting effects in melanoma cells, downmodulation of AR in dermal fibroblasts also results in cellular senescence and induction of SASP effector genes, which can be genetically dissociated from senescence by loss of p53¹⁶ or, as we have recently shown, by selective upregulation of an AR target with transcription co-regulatory function¹⁷.

A close interconnection exists between the senescence of stromal fibroblasts - connected with the aging process - and the induction of SASP consisting of the production of multiple pro-tumorigenic cytokines, matrix components and remodeling enzymes^{18,19}. These are also differentially upregulated in fully established CAF subpopulations, which have little or no signs of senescence and co-expand with cancer

¹Personalised Cancer Prevention Unit, ORL Service, Centre Hospitalier Universitaire Vaudois, Lausanne, Switzerland. ²Department of Immunobiology, University of Lausanne, Epalinges, Switzerland. ³Cutaneous Biology Research Center, Department of Dermatology, Massachusetts General Hospital and Harvard Medical School, Charlestown, MA, USA. ⁴Cancer Genomics Laboratory, Edo and Elvo Tempia Valenta Foundation, Biella, Italy. ⁵International Cancer Prevention Institute, Epalinges, Switzerland. ⁶Present address: Department of Biological Sciences, Birla Institute of Technology and Science (BITS) Pilani Campus, Pilani, India. ✉e-mail: soumitra.ghosh@pilani.bits-pilani.ac.in; gdotto@mgh.harvard.edu

cells^{11,20,21}. We have previously shown that AR plays a key role in the control of early steps of CAF activation, as a direct negative regulator of senescence and CAF/SASP effector genes^{16,20}. Decreased AR expression in human dermal fibroblasts (HDFs), as it can occur upon UVA exposure and in skin premalignant and malignant cancer lesions, leads to a senescence phenotype that can be overcome by concomitant down-modulation of p53, and induction of SASP/CAF effector genes and tumor enhancing properties that are unaffected by p53 loss. Downstream of this sequence of events, the identification of mechanism(s) that are involved in the activation of specific CAF subtypes would be of substantial interest to prevent the entire cancer process.

Mammalian cells express two types of nuclear lamins, which are key components of the scaffold around the nucleus^{22,23}. Nuclear lamins play an essential role at the level of the nuclear envelope and inside the nucleus, impacting on transcription, splicing, chromatin organization and DNA repair^{24,25}. While type B lamins can play an important role in many aspects of cell physiology, chromatin-related studies have focused on intranuclear localization and function of type A/C lamins^{22,24,26}. Though nuclear lamins have been highly studied in the context of aging and cancer²⁴, to our knowledge, their role in CAFs has not been investigated.

Here, we show that AR loss, by either genetic or pharmacological means, causes significant nuclear alterations in HDFs unlinked from p53-dependent cellular senescence, with similar abnormalities occurring in CAFs, which can be overcome by restored AR function. AR physically associates with lamin A/C and is a determinant of its proper localization at the nuclear membrane versus chromatin compartment. AR loss compromises the association of lamin A/C with the nuclear protein phosphatase PPP1 and results in increased lamin A/C phosphorylation at Ser 301, which is also a distinguishing feature of CAFs. Phospho-301 lamin A/C is recruited to the promoter/transcription regulatory region of CAF effector genes of the myofibroblast type and expression of phospho-mimetic (Ser/Asp) 301 lamin A/C mutant is sufficient to induce expression of these genes and trigger CAF activation without an impact on senescence. Thus, nuclear abnormalities and lamin A/C phosphorylation at a specific site are CAF features of functional significance resulting from the loss of AR.

Results

Nuclear membrane integrity depends on sustained AR expression in normal dermal fibroblasts

Loss of androgen receptor (AR) in human dermal fibroblasts (HDFs) triggers early steps of CAF activation, with induction of p53-dependent cellular senescence and expression of multiple CAF effector genes¹⁶. Lentiviral-mediated silencing of the *AR* gene in three different strains of HDFs resulted in consistent nuclear alterations, with irregular shape and decreased circularity index, membrane blebbing and micronuclei (MN) formation (collectively referred to as “nuclear abnormalities”) (Fig. 1A–C; Supplementary Fig. 1A, B). Transmission electron microscopy (TEM) of *AR*-silenced cells showed nuclear envelope invaginations, nuclear blebbing, and MN formation, which were not detectable in control cells (Fig. 1D, Supplementary Fig. 1C).

Similar nuclear abnormalities were observed in *AR* silenced HDFs cultured on collagen-coated soft surfaces (Supplementary Fig. 1D) and upon *AR* silencing in p53-knockdown HDFs (Supplementary Fig. 1E, F), indicating that the consequences of AR loss on nuclear structural integrity do not depend on substrate stiffness condition nor are linked to p53-dependent cellular senescence.

We sought validation of the results by deletion of the *AR* gene by CRISPR/Cas9 technology²⁷. Given the negative effects of *AR* loss in HDFs¹⁶, we resorted to infection of three different strains with high titer lentiviruses co-expressing Cas9 together with two different *AR*-targeting guide RNAs (gRNAs), followed by analysis of pooled polyclonal cell populations shortly after infection. Surveyor assays²⁸ and immunofluorescence staining with anti-AR antibodies indicated that the *AR*

gene was targeted and AR protein expression was effectively reduced by this approach in the majority of the cells (Supplementary Fig. 1G, H). Combined immunofluorescence and nuclear morphometric analysis showed that CRISPR-targeting of *AR* in HDFs resulted in similar nuclear alterations as upon shRNA-mediated gene silencing (Fig. 1E).

As an alternative pharmacological approach, HDFs were treated with two different AR inhibitors, one, ARCC4, causing PROTAC-mediated degradation of AR²⁹ and the other, AZD3514, suppressing AR activity through both ligand competitive and non-competitive mechanisms³⁰. Immunofluorescence analysis showed that treatment of multiple HDF strains with either inhibitor caused effective loss of AR expression that was accompanied by drastically increased nuclear alterations (Fig. 1F, Supplementary Fig. 1I).

The maintenance of nuclear membrane integrity is a dynamic process³¹. Time-lapse fluorescence microscopy of HDFs expressing a green fluorescent protein fused with a nuclear localization signal (GFP-NLS) revealed a highly dynamic pattern of nuclear blebbing in HDFs with the silenced *AR* gene, associated with transient nuclear envelope rupture during interphase (NERDI)³¹. A rapid decrease of nuclear GFP signal was observed in these cells that was followed by a gradual accumulation back into the nucleus upon nuclear membrane repair³¹ (Fig. 1G, H, Supplementary Fig. 1J). Permanent nuclear rupture was also observed in some of the cells (Fig. 1I, Supplementary Fig. 1J).

Thus, loss of AR expression in normal dermal fibroblasts results in compromised nuclear membrane integrity.

Nuclear abnormalities are an AR-dependent feature of CAFs

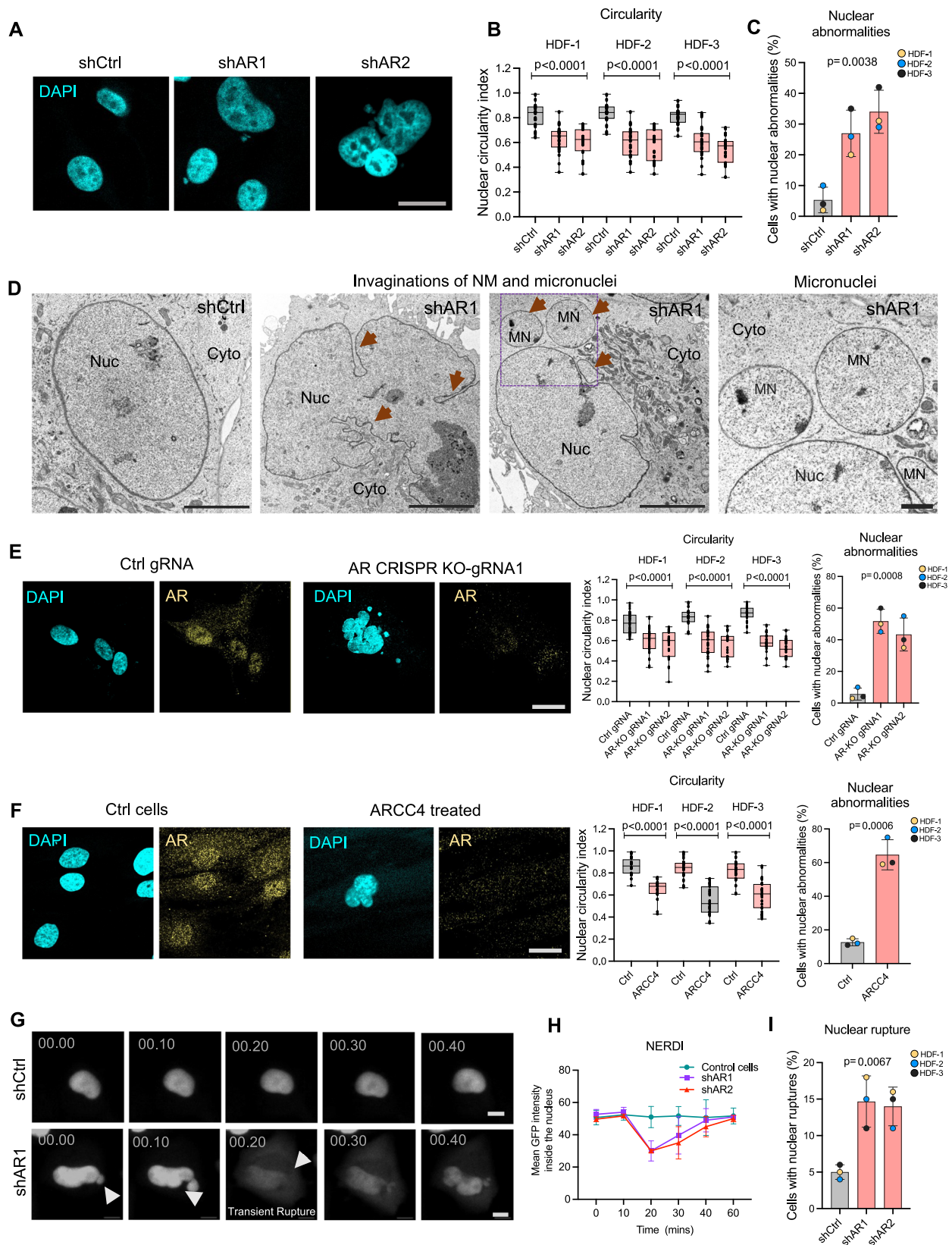
Decreased *AR* expression is a hallmark of CAFs, with CAF activation being counteracted by increased AR expression¹⁶. Nuclear changes comparable to those resulting from *AR* loss in HDFs were found in a panel of skin Squamous cell carcinoma (SCC)-derived CAFs compared to matched HDFs from flanking unaffected skin of the same patients (Fig. 2A, Supplementary Fig. 2A). Overexpression of *AR* in the CAFs rescued their nuclear abnormalities, linking altered nuclear structure in these cells to levels of *AR* expression (Fig. 2B, Supplementary Fig. 2B). AR can positively regulate its own expression as part of a positive feedback regulatory loop³². Treatment of CAFs with the AR agonist Ostarine³³ resulted in a concomitant increase of endogenous AR expression and suppressed nuclear abnormalities (Fig. 2C, D; Supplementary Fig. 2C).

To assess whether nuclear changes are also a feature of CAFs in vivo, we examined the nuclear shape of the fibroblasts within skin SCC lesions compared to fibroblasts from flanking unaffected skin in multiple patient-derived tissues. Double immunofluorescence analysis using antibodies against pan-keratin and vimentin was used to localize cancerous lesions and identify cell types (Fig. 2E; Supplementary Fig. 2D). Parallel sections were stained with antibodies against vimentin and AR with DAPI for nuclear visualization. Confocal microscopy and 3D reconstruction of multiple optical planes showed that decreased AR expression in SCC-associated fibroblasts was accompanied by significant changes in nuclear shape (decreased circularity) and abnormalities (increased blebbing, MN) (Fig. 2F–I, Supplementary Fig. 2E, F).

Thus, nuclear changes are an AR-dependent feature of clinically occurring CAFs and occur both in vitro and in vivo.

AR is a determinant of nuclear lamin A/C localization

Lamin A/C plays a prominent role both at the level of the nuclear envelope and inside the nucleus, in the control of gene transcription^{22,34,35}. Co-immunoprecipitation (Co-IP) and proximity ligation assays (PLAs) with antibodies against AR and lamin A/C showed an association of these proteins in HDFs, with positive PLA signals (puncta) being lost in cells with *AR* silencing (Fig. 3A, B, Supplementary Fig. 3A). Consistent with dual distribution of lamin A/C, PLA puncta resulting from AR-lamin A/C interactions were detected both at the nuclear membrane and in the nucleoplasm (Fig. 3B–D).



Number of PLA puncta was also drastically reduced in cells with degradation of the AR protein by a PROTAC-derived compound (ARCC4), while it was enhanced by treatment with the AR ligand dihydrotestosterone (DHT) that leads to increased AR expression (Fig. 3C, Supplementary Fig. 3B).

To assess whether AR and lamin A/C can bind directly to each other in the absence of ligand, we incubated purified recombinant His-

tagged AR protein, which lacks the ligand binding domain (UniProt: P10275-2; aa 1-560 amino acids), with full-length lamin A (Fig. 3E). Lamin A pull-down with anti-lamin A/C antibodies followed by immunoblotting showed effective binding of lamin A to the recombinant AR protein. AR/lamin A association was found to be lost when the AR protein was heat denatured prior to binding assay or when the binding reaction was performed in high salt (800 mM NaCl) buffer (Fig. 3E). By

Fig. 1 | Loss of AR in HDFs leads to nuclear membrane abnormalities and rupture. **A–C** Alterations of nuclear morphology in three primary HDF strains infected with two AR silencing lentiviruses (shARI and shAR2) versus control (shCtrl). **A** Representative images of DAPI-stained nuclei at 6 days post-infection. Scale: 10 μm . **B** Box whisker plots show the median circularity index in AR-silenced vs. control HDFs. The plot includes the minimum, first quartile (lower bound), median, third quartile (upper bound), and maximum values, whiskers down to the minimum and up to the maximum value. Dots indicate individual data points. Non-parametric one-way ANOVA, $n = 3$ conditions (51 cells per condition). **C** Percentages of cells with nuclear abnormalities (micronuclei and nuclear blebbing). Non-parametric one-way ANOVA, $n = 3$ strains (100 cells per condition), mean \pm SE. **D** Transmission Electron Microscopy images reveal nuclear membrane abnormalities (invaginations, micronuclei) in AR-silenced HDFs compared to controls. Scale: 5 μm (three left panels), 1 μm (right panel). Additional images are shown in Supplementary Fig. 1C. **E** Fluorescence images of DAPI-stained nuclei and AR immunostaining in HDFs infected with high titer lentiviruses expressing scrambled gRNA (Ctrl gRNA) or two independent AR-targeting gRNAs (gRNA1 and gRNA2). AR gene targeting and loss of AR expression are shown in Supplementary Fig. 1F, G. Box whisker plots show nuclear circularity, with minimum, first quartile (lower bound), median, third quartile (upper bound), maximum values, whiskers down to the minimum and up

to the maximum value, and dots for individual data points. Nonparametric one-way ANOVA, for circularity, $n = 56$ (HDF-1), $n = 55$ (HDF-2), and $n = 54$ (HDF-3) cells per condition. For abnormalities, $n = 3$ strains, mean \pm SE. Scale: 10 μm .

F Representative images and quantification of nuclear morphology in HDFs treated with AR degrading compound ARCC4 (1 μM for 72 h) versus control (EtOH). Box whisker plots show nuclear circularity, with minimum, first quartile (lower bound), median, third quartile (upper bound), maximum values, whiskers down to the minimum and up to the maximum value, and dots for individual data points. For circularity, $n = 64$ cells per condition; for abnormalities, $n = 3$ strains; paired t-test, mean \pm SE. Scale: 10 μm . **G** Representative snapshots from time-lapse imaging of control and shAR HDF cells, expressing GFP with nuclear localization signal (GFP-NLS). Cells were imaged every 10 min for 24 h. AR-silenced cells exhibited transient nuclear envelope rupture (NERDI), visible as nuclear blebs and rupture, followed by GFP-NLS recovery. Time (h:min); scale: 5 μm . **H** Kinetics of NERDI from GFP-NLS live-cell imaging of control and shAR HDF cells, with 10-min intervals. The graph indicates data obtained from the mean nuclear GFP signal intensity of 20 cells from each condition in three independent strains. Data are presented as mean values \pm SD. **I** Quantifications of the percentage of cells with nuclear envelope rupture in shCtrl, shARI, shAR2 conditions. Non-parametric one-way ANOVA, $n = 3$ strains, mean \pm SE. Source data for individual graphs are in the Source Data file.

further in vitro binding assays with truncated proteins, we show that the N-terminal domain (aa. 1-560) but not the ligand-binding C-terminal domain (aa. 699-920) of AR and the rod domain of lamin A/C are the ones mediating their association (Fig. 3F).

The AR-lamin A/C association is of functional significance. In fact, while total lamin A/C levels were unaffected by AR silencing (Supplementary Fig. 3C), immunofluorescence analysis showed a marked accumulation of lamin A/C in the nuclear interior of multiple HDF strains with silenced AR (Fig. 3G), with no significant change in lamin B1 distribution (Supplementary Fig. 3D). Nucleoplasmic accumulation of lamin A/C was also found by immunofluorescence analysis of CAFs compared to matched HDFs, which was reversed by overexpression of AR (Fig. 3H,I, Supplementary Fig. 3E,F).

Thus, AR associates with lamin A/C and is a determinant of its proper nuclear distribution in both HDFs and CAFs.

AR loss compromises lamin A/C association with the PPP1 phosphatase and induces lamin A/C phosphorylation at Ser 301

Localization and function of lamin A/C involve its association with a variety of proteins^{25,36,37}, which may be affected by loss of AR. We investigated this possibility by mass spectrometric analysis of lamin A/C immunoprecipitates from three different HDF strains plus/minus AR silencing. The association of lamin A/C with many proteins associated with the cytoskeleton, nuclear pore and importin complexes was consistently reduced by AR loss, together with enzymes involved in chromatin modification and RNA metabolism (Fig. 4A, Supplementary Data S1). Mass spectrometry also demonstrated a consistent decrease in the interaction between lamin A/C and three catalytic subunits of protein phosphatase 1 (PPP1C-A, B, C) as well as a regulatory subunit (PPP1R18) in HDFs with silenced AR (Fig. 4A; Supplementary Data S1). The AR-dependent association of lamin A/C with PPP1 was independently confirmed by co-immune precipitation and PLA assays with antibodies against lamin A/C and PPP1C/B in HDFs with silenced AR versus controls (Fig. 4B,C, Supplementary Fig. 4A). PLA assays also showed a marked reduction of lamin A/C-PPP1 puncta in HDFs treated with the AR-degrading ARCC4 compound versus ethanol control (Supplementary Fig. 4B). Besides associating with nuclear lamins³⁸, PPP1 has been previously reported to associate with AR³⁹, a finding that we also obtained with HDFs, by initial Mass Spec analysis of AR immunoprecipitates and directly verified by PLA assays (Supplementary Fig. 4C). The specific subunits of PPP1 involved and the possibility of a tripartite complex of these proteins will have to be separately pursued by dedicated biochemical/structural studies.

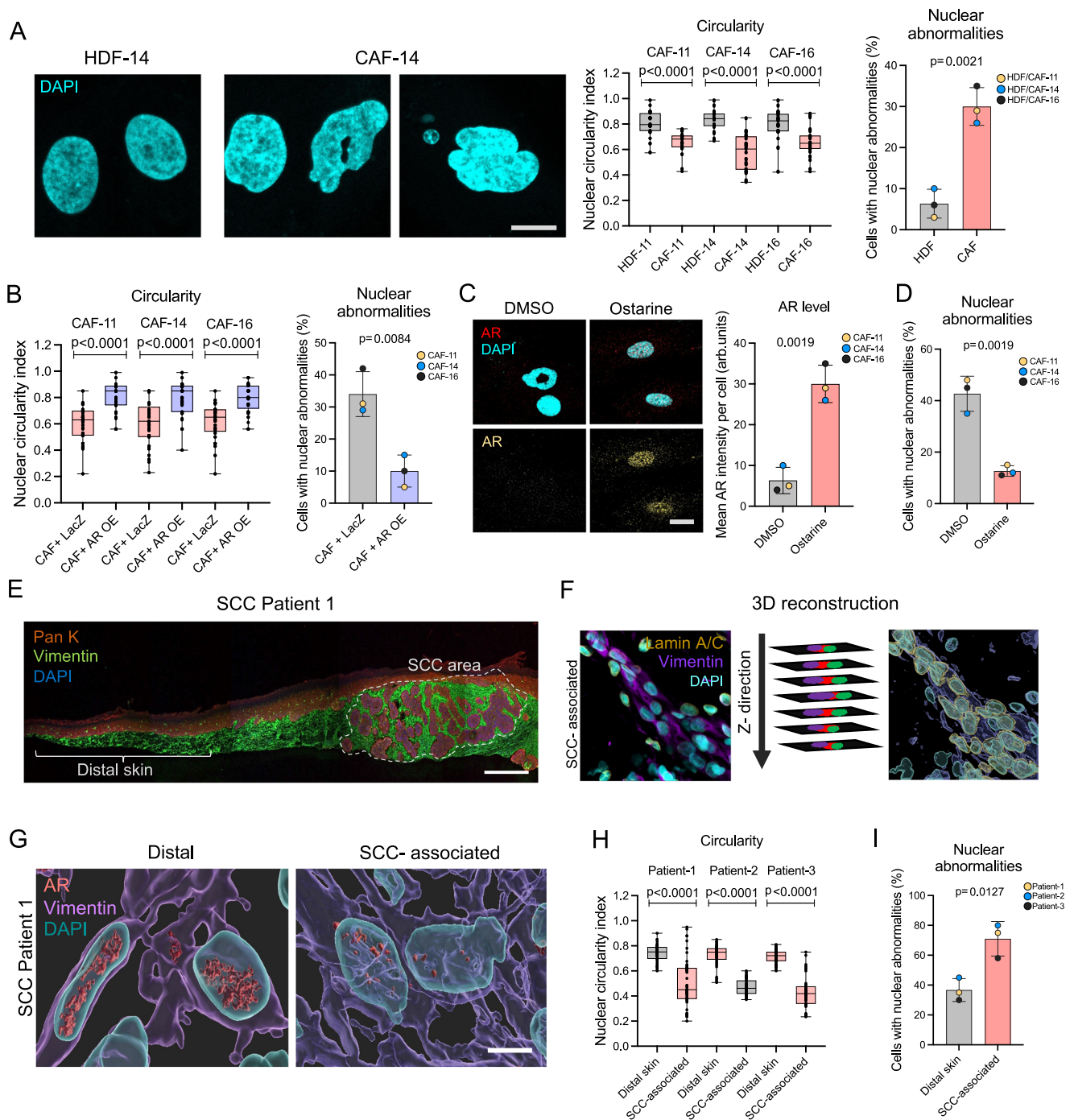
PPP1 is involved in control of lamin A/C phosphorylation^{38,40}, which is, in turn, a key determinant of its localization and function⁴¹. A number of phosphorylated sites were detected in the mass spectra profiles of lamin A/C immunoprecipitates, among which phosphorylation at Ser 301 was consistently enriched in all three HDF strains with silenced AR compared to control (Supplementary Fig. 4D, Supplementary Data S2). Immunoblot analysis with phospho-specific antibodies showed a marked increase in lamin A/C phosphorylation at Ser 301 in HDFs treated with the AR inhibitors AZD3514 and ARCC4 (Fig. 4D). The induction of Ser301 phosphorylation was confirmed by immunofluorescence analysis of several HDF strains treated with the ARCC4 compound in parallel with the PPP1 inhibitor tautomycin⁴² (Fig. 4E, Supplementary Fig. 4E), and was similarly observed upon AR silencing in multiple HDF strains (Fig. 4F, Supplementary Fig. 4F). 3D surface reconstruction of confocal Z-stack images showed that phospho-Ser301-lamin A/C induced by AR silencing localizes to the nuclear interior, while total lamin A/C is also present at the membrane (Fig. 4G).

Thus, loss of AR in HDFs impairs lamin A/C association with the PPP1 phosphatase and results in increased lamin A/C phosphorylation at Ser301.

Lamin A/C phosphorylation at Ser301 is a feature of CAFs

An important question was whether the observed increase(s) in lamin A/C phosphorylation at Ser301 also occurs in CAFs. Immunofluorescence analysis using phospho-specific antibodies revealed a substantial elevation of Ser301 phosphorylation, with pronounced nucleoplasm distribution, in several CAF strains compared to matched HDFs from the same patients (Fig. 5A, Supplementary Fig. 5A). In parallel with the restored nuclear shape, Ser301 phosphorylation was significantly reduced by treatment of CAFs with the AR agonist ostarine (Fig. 5B), with a concomitant increase in PPP1-lamin A/C association (Supplementary Fig. 5B).

Next, we extended the analysis to clinical skin lesions by immunofluorescence with antibodies against phospho-Ser301 lamin A/C and various markers of fibroblast and CAF subpopulations. We found increased levels of nuclear phospho-Ser301 staining in SCC-associated fibroblasts positive for PDGFR- α and vimentin relative to fibroblasts of distal unaffected skin (Fig. 5C, D, F; S5C, D). Levels of phospho-Ser301 staining in SCC-associated fibroblasts positive for the PDGFR- α and vimentin markers were similar to those in cells in the same lesions positive for specific CAF markers like α -SMA, FAP and tenascin, which were not detected in the fibroblasts of distal unaffected skin (Fig. 5E, F; S5D–F). Confocal microscopy followed by 3D reconstruction



confirmed these findings, showing a pronounced intranuclear distribution of phospho-Ser301 lamin A/C in SCC-associated fibroblasts (Fig. 5G). PLA in tissues demonstrated a significant reduction in lamin-PPPIA/B association in SCC-associated fibroblasts compared to fibroblasts in distal unaffected skin from the same patients (Fig. 5H).

Thus, increased lamin A/C phosphorylation at Ser301 is a feature of CAFs in vitro and in vivo, which is accompanied by impaired lamin A/C-PPPI association.

AR loss results in enhanced binding of phospho-Ser 301 lamin A/C to CAF effector genes in concomitance with chromatin activation

Polymeric lamin A/C is known to interact with large heterochromatin domains called lamina-associated domains (LADs)⁴³, while dimeric nucleoplasmic lamin A/C can bind to a number of genomic sites

characteristic of active enhancers⁴⁴. LAD formation was investigated by Enriched Domain Detector (EDD) analysis⁴⁵ of lamin A/C ChIP-seq profiles of HDFs following high stringency nuclear extract conditions to improve detection of stronger DNA-lamin association⁴⁶. As shown in Supplementary Fig. 6A, the experimentally determined distribution of LADs in HDFs was matching that of previously reported LADs of IMR90⁴⁵, with only minimal changes occurring in smaller LADs in HDFs with silenced AR.

To assess to which extent AR loss leads to changes in chromatin association of nucleoplasmic lamin A/C, two different HDF strains plus/minus AR silencing were analyzed by ChIP-seq with antibodies against total and phospho-Ser301 lamin AC under less stringent condition. Consistent with the observed increase in lamin A/C nucleoplasmic localization and Ser301 phosphorylation, ChIP-seq analysis revealed a large increase of narrow peaks with antibodies against both

Fig. 2 | Nuclear abnormalities in cancer-associated fibroblasts (CAFs). **A Left:** Representative confocal images of DAPI-stained nuclei from CAFs and matched HDFs isolated from the same patients. Scale: 10 μ m. **Middle:** Box whisker plots show nuclear circularity, with minimum, first quartile (lower bound), median, third quartile (upper bound), maximum values, whiskers down to the minimum and up to the maximum value. Two-tailed paired t-test, $n = 51$ cells per condition. **Right:** Quantification of nuclear abnormalities in three pairs of CAFs and matched HDFs. Two-tailed unpaired t-test, $n = 3$ HDF strains, Mean \pm SE. Additional images are shown in Supplementary Fig. 2A. **B** Quantification of nuclear circularity index and nuclear abnormalities in three CAF strains infected with either a LacZ control (LacZ) or AR overexpressing lentivirus (AR OE). Cells were stained with DAPI and anti-AR antibody to determine nuclear morphology, and AR expression as shown in Supplementary Fig. 2B. Box whisker plots show nuclear circularity, with minimum, first quartile (lower bound), median, third quartile (upper bound), maximum values, whiskers down to the minimum and up to the maximum value, and dots for individual data points. Two-tailed paired t-test, $n = 63$ (CAF-11), $n = 61$ (CAF-14), and $n = 54$ (CAF-16) cells per condition. **Right:** Quantification of nuclear abnormalities, two-tailed unpaired t-test, $n = 3$ HDF strains, Mean \pm SE. Representative images and quantification of AR protein levels after AR- and DAPI-staining (**C**) and nuclear abnormalities (**D**) of three CAF strains treated with DMSO or Ostarine (10 μ M) for 48 h. Two-tailed unpaired t-test, $n = 3$ strains, Mean \pm SE. Scale: 10 μ m. **E** Immunofluorescence staining of excised skin SCC lesions with anti-pan-keratin

and anti-vimentin antibodies, and DAPI for nuclei identification. Areas of analysis were indicated by white dotted lines for SCC lesion and solid lines for unaffected skin. Scale: 100 μ m. This experiment was repeated on two additional patient samples shown in Supplementary Fig. 2D. Parallel sections were stained with anti-vimentin and anti-AR antibodies for the analysis shown in (**G**) and with anti-vimentin, anti-lamin A/C and anti-phospho-Ser301 antibodies, shown in Fig. 5E. **F** Schematic representation of 3D reconstruction of Z-stack confocal images derived from the SCC versus distal skin areas indicated in the previous panel. **G** 3D surface reconstruction images of DAPI-stained nuclei (cyan) of vimentin-positive fibroblasts (violet) concomitantly stained with anti-AR antibodies (red) from the SCC versus distal skin areas shown in (**E**). Scale: 5 μ m. Quantification of (**H**) nuclear circularity index and (**I**) nuclear abnormalities in fibroblasts from SCC-associated versus distal skin, of three patient-derived skin SCCs. Quantifications are based on 3D image reconstructions and volume rendering of DAPI-stained nuclei using the Imaris software package. Box-whisker plots show minimum value, first quartile (lower box bound), median (center), third quartile (top box bound), maximum value, whiskers down to the minimum and up to the maximum value. Two-tailed paired t-test, $n = 40$ cells per condition. For abnormalities, two-tailed unpaired t-test $n = 3$ HDF strains, mean \pm SE. Images of patient #2, and quantification levels of AR expression are shown in Supplementary Fig. 2E, F. Source data for individual graphs are in the Source Data file.

total and phospho-Ser301 lamin A/C in the two HDF strains with silenced *AR* versus controls (Fig. 6A, Supplementary Data S3). Distribution analysis showed that heightened binding peaks encompassed promoter, intronic and distal intergenic regions (Fig. 6B). Around the transcription Start Sites (TSS) of genes, *AR* silencing in both HDF strains resulted in higher and sharper binding peaks of total and phospho-Ser301 lamin A/C (Fig. 6C,D; S6B). In both strains we observed increased binding of total and phospho-Ser301 lamin A/C to a significant fraction of genes modulated by *AR* silencing, with a pronounced preference for the promoter and intronic regions of the up-regulated relative to the down-modulated genes (Fig. 6E, S6C). Many of the phospho-Ser301 lamin A/C bound genes up-regulated by *AR* silencing are of known functional significance, including several with a reported role in CAF activation (Fig. 6F).

The identification of overlapping ChIP-seq peaks with antibodies against different proteins depends on various parameters and software packages used for calculations of peak intensity and distribution⁴⁷. For further detailed analysis of binding distribution of total and phospho-lamin A/C we focused on individual CAF effector genes uploading their ChIP-seq profiles onto the Easeq tool (<https://easeq.net/>). As a point in case, we examined genomic regions encompassing the *TGFBR1* gene, whose expression and function are enhanced in CAFs^{5,48}. *AR* silencing in both HDF strains resulted in a notable increase of phospho-Ser301 lamin A/C binding peaks at a region encompassing the TSS of the gene and overlapping with peaks of H3K27Ac binding, a marker of open chromatin configuration⁴⁹, and chromatin accessibility (ATAC peaks) (Fig. 6G). There were only limited changes in total lamin A/C binding peaks, less clustered and coinciding to a limited extent with those of phospho-Ser301 (Fig. 6G). A similar increase and redistribution of phospho-lamin A/C binding peaks were found in HDFs with silenced *AR* at the promoter/transcription regulatory regions of other CAF effector genes under *AR* control, such as one for the matrix remodeling protein *PLOD2* (Fig. 6G) and those coding for immune modulators (*IL11*, *CXCL5*)^{50–52} (Supplementary Fig. 6D).

The “cut and run” technique provides an alternative to traditional ChIP-seq analysis, which does not require crosslinking of chromatin but relies on the direct incubation of nuclei with antibodies against target proteins, coupled with micrococcal nuclease for bound DNA fragmentation and sequencing⁵³. Using this method, we confirmed a significant increase of phospho-Ser 301 binding to the promoter region of a number of CAF effector genes in HDFs with silenced *AR*, while total

lamin A/C binding was less affected (Supplementary Fig. 7A). Increased phospho-Ser 301 binding to the promoter regions of selected CAF effector genes was further validated by direct ChIP-qPCR assays (Supplementary Fig. 7B).

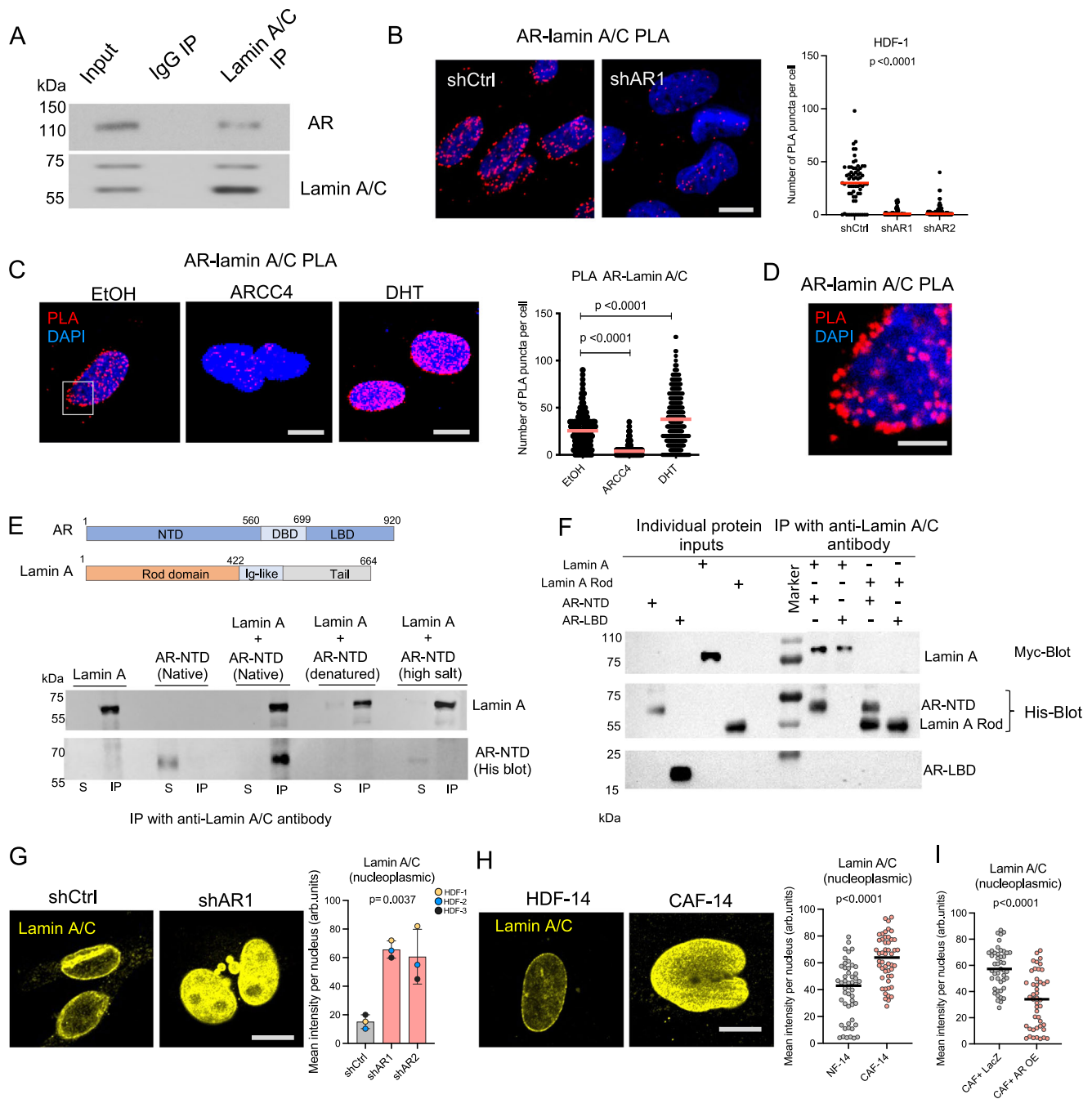
Thus, *AR* silencing in HDFs results in changes in chromatin activation associated with enhanced phospho-Ser301 lamin A/C binding of likely significance for CAF activation.

Expression of a phosphomimetic Ser 301 lamin A/C mutant is sufficient to trigger CAF activation unlinked from stromal fibroblasts senescence

To probe into the specific consequences of lamin A/C Ser 301 phosphorylation, we expressed a phosphomimetic Ser 301 to Asp (S301D) mutant and wild-type (WT) lamin A/C as GFP fusions. Infection of multiple HDF strains with lentiviruses expressing the S301D mutant or wild-type lamin A/C had no effects on proliferation and did not induce the senescence-associated changes in cell morphology that are observed upon *AR* gene silencing¹⁶ (Supplementary Fig. 8A).

There were no significant changes in the nuclear shape of HDFs expressing either the S301D mutant or WT lamin A/C (Supplementary Fig. 8B). GFP tagging of the two proteins enabled us to assess their distribution. As with endogenous phospho-Ser301 lamin A/C, the S301D mutant was found to localize predominantly to the nuclear interior, while wild-type lamin A/C was peripherally localized (Supplementary Fig. 8B, C). Concomitant IF analysis with antibodies against the CAF marker α -SMA showed that it was selectively induced in the S301D expressing HDFs (Supplementary Fig. 8B, C). RT-qPCR analysis showed that expression of the S301D mutant induced several other CAF effector genes without up-regulating *CDKN1A*, a determinant of senescence induced by *AR* silencing in these cells¹⁶ (Supplementary Fig. 8D). Similar increase in CAF effector gene was also observed upon overexpression of the S301D mutant in *TP53* silenced HDFs (Supplementary Fig. 8E). Parallel ChIP assays with anti-GFP antibodies showed selective binding of the S301D lamin A/C mutant to the promoter regions of various CAF effector genes (Supplementary Fig. 8F), which were also found to be bound by endogenous phospho-Ser301 in HDFs with silenced *AR* (Supplementary Fig. 7B).

More general, global transcriptomic analysis showed consistent changes in gene expression with the upregulation of many CAF effectors in two different HDF strains expressing the S301D mutant versus wild-type lamin A/C (Fig. 7A; Supplementary Data S4). We observed a significant overlap between phospho-Ser301 binding peaks



in AR silenced HDFs and the transcriptome resulting from S301D (Supplementary Data S4). The genomic distribution of these peaks revealed binding occurrences in various genomic regions, including promoters, introns, exons, and distal intergenic regions, associated with both up- and downregulated genes by AR (Fig. 7B). Approximately, 20% of genes up- and down-regulated by AR gene silencing were similarly modulated by S301D mutant expression, which belong to several categories of functional significance (Fig. 7C, Supplementary Data S5).

Gene set enrichment analysis (GSEA) revealed that profiles of HDFs expressing the S301D mutant were significantly enriched for gene signatures related to CAF activation of the matrisome and myofibroblast types^{11,54} (Fig. 7D, E). A signature of up-regulated genes in HDFs with S301D lamin A/C mutant expression was established (Supplementary Data S4) and used to analyze scRNA-seq datasets of skin Bowen's disease and cutaneous SCC compared to the healthy skin⁵⁵. We found a strong association of a gene signature of 200 upregulated

genes in S301D expressing HDFs which overlaps with that of cells positive for a CAF gene signature, which is much less evident in profiles of normal fibroblasts (Fig. 7F, G). We expanded the analysis to an additional single-cell RNA-seq profiles of head and neck squamous cell carcinoma (HNSCC)⁵⁶, finding a high signature score for S301D up-regulated genes specifically in the CAF and myofibroblast subpopulations (Fig. 7H).

A key property of CAFs is to enhance the proliferation and tumorigenicity of neighboring cancer cells. In co-culture assays in thin Matrigel layers¹⁶, expansion of squamous cell carcinoma (SCC13) cells was enhanced in the presence of HDFs with expression of the S301D mutant versus wild-type lamin A/C (Fig. 8A), with similar enhancing properties occurring in 3D spheroid forming assays (Fig. 8B). *in vivo* tumor-promoting activity was assessed by an orthotopic model of skin cancer formation based on intradermal injections of cells in Matrigel in the back skin of mice. As shown in Fig. 8C, SCC13 cells in combination with HDFs expressing the S301D mutant formed tumors of

Fig. 3 | AR is a determinant of nuclear lamin A/C localization.

A Immunoprecipitation of HDF cell lysates with anti-lamin A/C antibodies versus nonimmune IgGs followed by SDS-PAGE together with total lysate input and sequential immunoblotting with anti-AR and anti-lamin A/C antibodies. **B** Representative images (left) of proximity ligation assays (PLA) with antibodies against AR and lamin A/C in HDFs plus/minus AR silencing. Red fluorescence puncta resulting from the juxtaposition of anti-AR and lamin A/C antibodies were visualized by confocal microscopy with DAPI nuclear staining (blue). Scale: 5 μ m. Right: Quantification of number of puncta per cell with mean as red bar. Nonparametric one-way ANOVA test, $n = 65$ cells per condition. PLAs with two additional strains are provided in Supplementary Fig. 3A. **C** Representative images (left) of AR-lamin A/C PLA in HDFs treated with ethanol (EtOH), the AR-degrading compound ARCC4 (1 μ M) or AR agonist DHT (10 nM) for 72 h. Scale: 5 μ m. Right: Quantification of PLA puncta per cell, with mean as red bar. Two-tailed paired t-test, $n = 348$ cells per condition. Impact of ARCC4 and DHT treatment on levels of AR expression, is shown in Supplementary Fig. 3B. **D** Zoomed-in image of a nucleus of Fig. 3C (boxed) and distribution of the AR-lamin A/C PLA puncta both within the nucleus and nuclear periphery. Scale: 2 μ m. **E** Top: Schematic representation of domain structure of AR and lamin A proteins. Bottom: *in vitro* interaction assay of AR and lamin A. Recombinant full-length lamin A protein (Lamin A) was admixed with His-tagged AR-NTD protein (aa 1-560 aa) under native conditions. AR was previously denatured by a brief heat treatment (20 min at 85 $^{\circ}$ C), or proteins were incubated in

high salt buffer (800 mM NaCl) as specificity controls. Immunoprecipitates with anti-lamin A/C antibodies in parallel with 5% of the unbound supernatants were analyzed by immunoblotting with anti-lamin A/C or anti-His antibodies. The experiment was performed once. **F** *in vitro* interaction of individual domains of AR and lamin A protein. Recombinant myc-tagged full-length lamin A protein (lamin A) or His-tagged Lamin A Rod domain (Lamin A Rod) was admixed with either His-tagged AR-NTD protein or AR-LBD protein under native conditions. Immunoprecipitates with anti-lamin A/C antibodies in parallel with individual purified proteins were analyzed by immunoblotting with HRP conjugated anti-myc, anti-His and anti-AR-LBD antibodies, respectively. The experiment was performed more than once. **G** Immunofluorescence analysis of lamin A/C localization in three HDF strains plus/minus AR silencing. Representative images (left) and quantification of nucleoplasmic lamin A/C fluorescence signal intensity expressed in arbitrary units (right). Non-parametric one-way ANOVA, $n = 3$ strains (50 cells per condition), mean \pm SE. Scale: 10 μ m. **H** Comparison of nucleoplasmic lamin A/C fluorescence intensity between CAFs and matched HDFs from the same patients, with mean as black bar. Two-tailed unpaired t-test. $n = 50$ cells per condition. Scale: 5 μ m. Data for additional strains are shown in Supplementary Fig. 3E. **I** Quantification of nucleoplasmic lamin A/C fluorescence intensity in CAFs infected with LacZ control or AR-over-expressing lentivirus, with mean as black bar. Two-tailed unpaired t-test, $n = 50$ cells per condition. Source data for relevant panels are in the Source Data file.

significantly larger size than with HDFs expressing wild-type lamin A/C. Lesions formed in the presence of S301D-expressing HDFs were characterized by greater density of SCC cells (expressing the RFP marker) with an increase of α -SMA positive fibroblasts (Fig. 8D, E).

Thus, expression of a phospho-mimetic Ser 301 lamin A/C mutant in HDFs is sufficient to induce a transcriptional program of CAF activation and confer on cells growth- and tumor-enhancing properties.

Discussion

CAFs are key determinants of the cancer process, from initiation to metastatic spread^{7,57}. Resident stromal fibroblasts are a primary source of CAFs, with a plastic response to various cues resulting in CAF subpopulations with distinct functions^{5,7-11}. The androgen receptor (AR) represses a senescence program of gene transcription associated with early steps of CAF activation and acts as a master negative regulator of CAF effector genes¹⁶. Here we have uncovered a novel role of AR as a determinant of nuclear envelope integrity, lamin A/C distribution, phosphorylation, and transcription modulatory function of relevance for CAF activation.

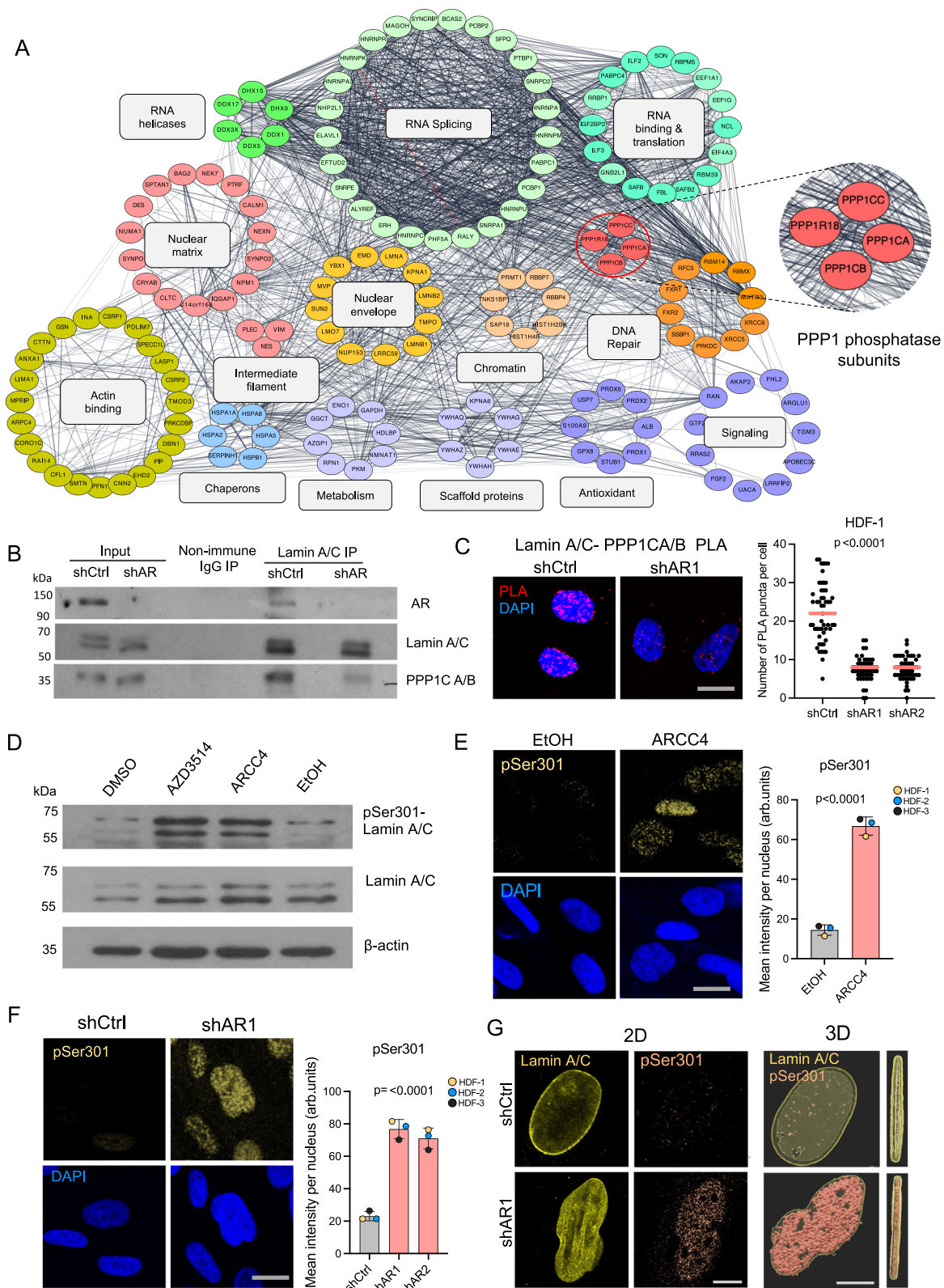
As overviewed in the introduction, cumulative evidence from our laboratory indicates that AR plays a dual role in skin cancer that is closely intertwined but can be genetically dissociated from that of senescence. Control of AR expression is a point of convergence of multiple mechanisms, which are better studied in prostate cancer^{58,59}, but also emerging in other cancer types such as melanoma, in which AR positively regulates its own expression as part of an adaptive mechanism to targeted therapy⁶⁰. UVA exposure, a main cause of skin aging¹¹ and cancer risk¹² can directly reach the dermal compartment of normal skin, and suppress AR expression in dermal fibroblasts¹⁶. While underlying mechanisms remain to be determined, decreased AR expression is also found in fibroblasts underlying premalignant skin cancer lesions and in CAFs, in which AR expression can be restored by agonist treatment. Given the dual role of AR in skin cancer, the identification of selective modulators of AR expression and activity in the dermal fibroblast versus cancer cell compartment will be invaluable to diminish the cancer risk.

Conversion of tissue-resident fibroblasts into CAFs can be viewed as a multistep process, with an early phase, closely intertwined with senescence and SASP induction²⁰, and a second one, unlinked from senescence and leading to establishment of various CAF subpopulations with different roles within tumors^{5,7-11}. Our evidence indicates that downmodulation of AR expression, as it can already occur in

photoaged skin before overt tumor formation¹⁶, is a determinant of the first set of events, while more specific mechanisms downstream of AR loss are involved in the second. In fact, we have recently shown that decreased AR expression in HDFs triggers a transcriptional program of both profibrotic and inflammatory CAF subpopulations, while upregulation of the transcriptional co-activator ANKRD1, resulting from AR loss, is selectively involved in induction of profibrotic CAF phenotype¹⁷. In the present work, we have found that induction of lamin Ser301 phosphorylation by loss of AR is also selectively involved in control of CAF effector genes of the matrisome - profibrotic type. Taking a broader, “reverse” functional approach, we previously showed that induction of the profibrotic versus inflammatory CAF subpopulations can be recapitulated by differential modulation of the transforming growth factor-beta (TGF- β) versus fibroblast growth factor (FGF) signaling pathways^{17,18}, which will be very interesting to connect in future studies with the AR-lamin A/C interplay that we have uncovered.

An involvement of AR in the maintenance of nuclear structure, to our knowledge, has not been previously reported. We have shown that AR loss in normal dermal fibroblasts by either genetic or pharmacologic approaches results in significant deformation of nuclear shape, nuclear abnormalities (blebbing, MN formation) and ruptures during interphase. These are also a feature of CAFs, both in culture and in cancer lesions, which can be counteracted by increased AR expression. By analogy with what has been proposed for cancer cells^{3,61,62}, nuclear abnormalities can contribute to alterations in gene expression and tumor enhancing properties of CAFs as we have experimentally observed.

UVA is a potent inducer of cellular stress that can reach directly cells of the dermal compartment and plays a key role in cancer risk⁶³. No significant changes in nuclear circularity index were detected in a time course of UVA treatment of HDFs at a dose resulting in persistent induction of p21^{WAF1/Cip1} expression as a marker of stress-induced p53 activity (Supplementary Fig. 9A, B). Thus, nuclear alterations resulting from AR loss cannot be simply attributed to a general cellular stress response and it will be interesting to determine to which extent other perturbations connected with changes in nuclear morphology⁶⁴ involve an AR-dependent mechanism. Here, we note that similar nuclear abnormalities have been observed upon short term treatment of HDFs with AR inhibitors and degraders as after AR silencing or deletion, indicating that they are an early consequence of AR loss. The nuclear membrane abnormalities are also reversible, as they could be



normalized in CAFs by ectopic *AR* expression and by treatment with Ostarine (also known as MK-2866 or Enobosarm)^{65,66}, a selective androgen receptor modulator (SARM) that in our system functions as a full *AR* agonist, capable to induce endogenous *AR* levels as well as downmodulate CAF effector genes¹⁷.

To assess whether nuclear abnormalities induced by *AR* loss are fibroblast specific, we examined two prostate cancer cell lines, LNCaP and PC3, as well as melanoma cells. Silencing of *AR* resulted in a two

fold increase of nuclear abnormalities in LNCaP prostate cancer cells, which express high levels of *AR* and *AR*-dependent in their growth, while lesser effects were observed with PC3 cells, which are characterized by low levels of *AR* expression and are not *AR*-dependent⁶⁷ (Supplementary Fig. 9C, D). The analysis was extended to two melanoma cell lines (A375 and SK-MEL-28) that express *AR* and are growth suppressed upon *AR* knockdown¹⁴. *AR* silencing in both cell lines resulted in a strong induction of nuclear abnormalities

Fig. 4 | Loss of AR compromises the association of lamin A/C with the phosphatase PPP1 and results in increased lamin A/C phosphorylation at Ser 301. **A** Cytochrome network of proteins with reduced association with lamin A/C in AR-silenced HDFs. Proteins were identified by LC-MS/MS analysis from three different HDF strains with/without AR silencing. The list of interactors is shown in Supplementary Data S1. Names of proteins with reduced association (log fold change >1.5) in at least two strains are displayed. The inset shows PPP1 subunits associated with lamin A/C in an AR-dependent manner. **B** Co-immunoprecipitation assays with HDFs plus/minus AR silencing with anti-lamin A/C antibodies or nonimmune IgGs followed by immunoblotting with anti-AR, -lamin A/C, and -PPP1CA/B antibodies, with parallel analysis of the inputs. **C** PLA with anti-lamin A/C and PPP1CA/B antibodies of HDFs plus/minus AR silencing. Shown are representative images and quantification of the number of puncta per cell, with the mean value as red bar. Non-parametric one-way ANOVA, $n = 53$ cells per condition. Scale: $10\ \mu\text{m}$. **D** Immunoblot analysis of HDFs treated with ARCC4 ($1\ \mu\text{M}$) or AZD3514 ($10\ \mu\text{M}$) for 72 h, with phospho-Ser301 lamin A/C, total lamin A/C, and β -Actin antibodies.

E Immunofluorescence analysis of three HDF strains treated with ARCC4 ($1\ \mu\text{M}$) or EtOH for 72 h, antibodies against phospho-Ser301-lamin A/C (yellow), and DAPI for nuclear staining. Representative images (left) and fluorescence signal intensity quantification (right), Two-tailed unpaired t-test, $n = 3$ strains (50 cells per condition), mean \pm SE. Scale: $10\ \mu\text{m}$. **F** IF analysis of three HDF strains, infected with AR-silencing lentiviruses versus control, with antibodies against phospho-Ser301(p-Ser301)-lamin A/C (yellow) and counterstained with DAPI. Representative images (left) and fluorescence intensity quantification (right), nonparametric one-way ANOVA, $n = 3$ strains (50 cells per condition), mean \pm SE. Scale: $10\ \mu\text{m}$. Fluorescence intensities per individual counted cells for each strain are shown in Supplementary Fig. 4D. **G** 3D Surface Reconstruction: Whole nuclei of HDFs plus/minus AR silencing stained with anti-phospho-S301-lamin A/C (red) and total lamin A/C (yellow). Z-stacks of confocal images used for 3D volumetric reconstruction with Imaris Surface tool. 2D and 3D images of Lamin A/C and pSer301 signals; top and lateral views. Scale: $5\ \mu\text{m}$. Source data for individual graphs are in the Source Data file.

(Supplementary Fig. 9E, F). Mirroring the HDF findings, PLAs demonstrated the association between AR and lamin A/C (Supplementary Fig. 9G) and IF analysis revealed that AR silencing resulted in the mislocalization of lamin A/C to the nucleoplasm (Supplementary Fig. 9H). Thus, AR plays an important role in maintaining nuclear structure across diverse cell types, which can be mediated, at least in part, by its interaction with lamin A/C as discussed below.

Molecularly, we found that AR binds to nuclear lamin A/C and ensures its proper localization and association with proteins involved in nuclear membrane composition and connection with the cytoplasm. Mass Spec analysis of multiple HDF strains revealed that the association of many of these proteins with lamin A/C was consistently decreased upon AR silencing. For further biochemical and functional studies, we focused on the AR-dependent association of lamin A/C with the PPP1 phosphatase, given its potentially broader involvement in the modulation of lamin A/C function^{38,40}.

Phosphorylation of nuclear lamins controls multiple aspects of their function, including depolymerization at the onset of mitosis, subnuclear distribution during interphase, chromatin organization, and gene transcription³⁴. The impact that changes in lamin A/C phosphorylation have on CAF activation, to our knowledge, has not been explored. A number of different kinases including PKC, MAPK, and Akt have been shown to phosphorylate lamins at different sites, leading to different outcomes that are better characterized in relation to the cell cycle³⁴. The PPP1 and PPP2 phosphatases have been implicated in the dephosphorylation of lamins, specifically in post-mitotic cells⁶⁸.

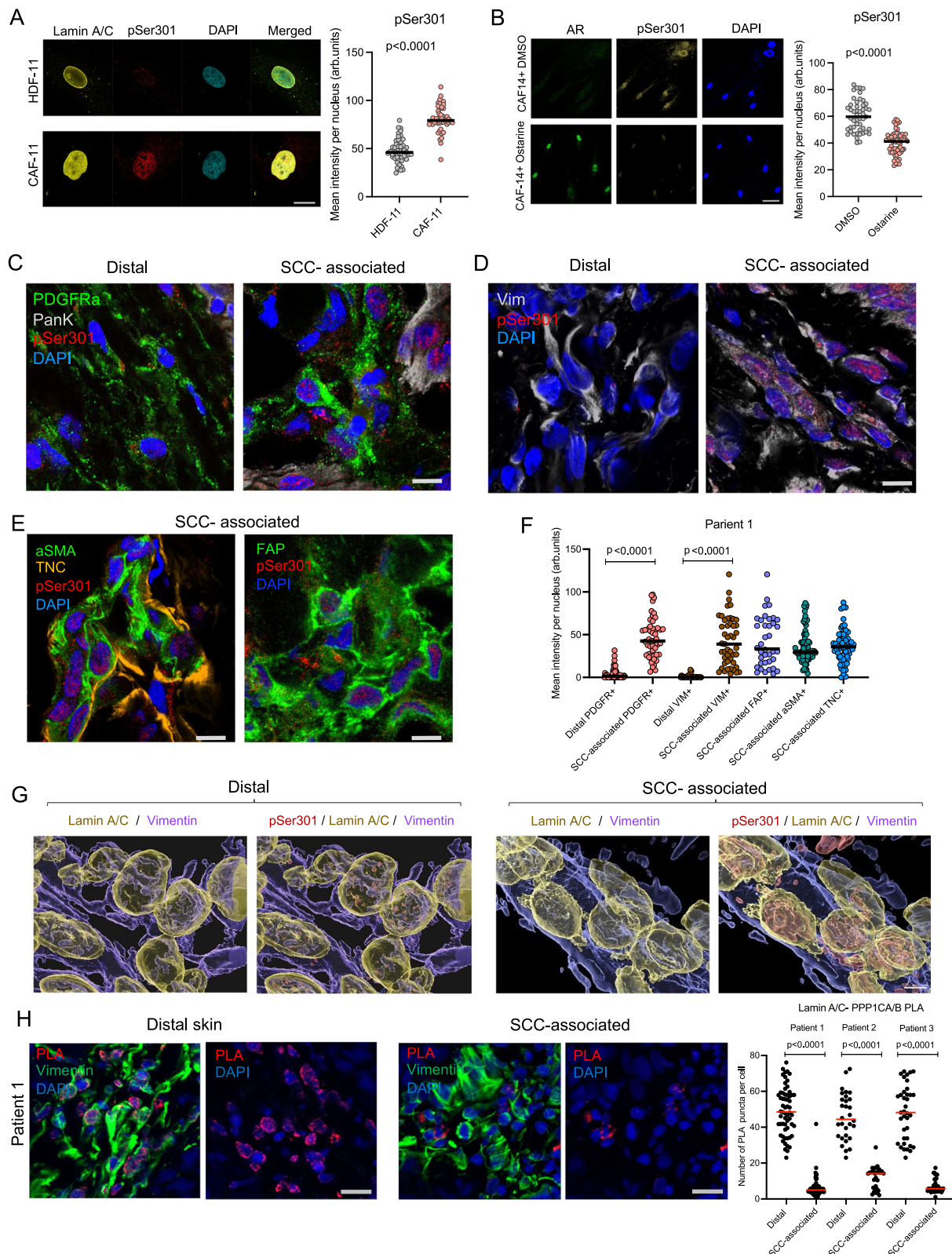
PPP1 is composed of multiple catalytic (PPP1CA, PPP1CB and PPP1CC) and regulatory subunits implicated in target specificity⁶⁹. In our experimental setting, we detected association of lamin A/C with multiple PPP1 subunits and found it to be significantly compromised by AR gene silencing or PROTAC-mediated AR degradation. Concomitantly, loss of AR resulted in a marked increase of lamin A/C phosphorylation at Ser 301, which was also observed upon PPP1 inhibition. Phosphorylation of lamin A/C at another residue implicated in the cell cycle, Ser22⁴⁴, was observed in HDFs upon AR gene silencing but not PROTAC-mediated degradation, indicating that it is a more indirect consequence of AR loss (Supplementary Fig. 4F, G). Increased phosphorylation at Ser301, but not Ser22, together with reduced lamin A/C - PPP1 association, was also observed in CAFs, in culture and in clinically occurring lesions, in vivo. The significance of lamin A/C phosphorylation at Ser 301, as reported in one study by the Akt kinase⁷⁰, has been explored to a very limited extent. By the combination of biochemical and direct functional approaches discussed below, we have shown that this modification is of importance for the transcriptional program of CAF activation.

Nuclear lamins have been extensively studied for their contribution to the control of gene expression through both direct and indirect mechanisms. LADs are global determinants of chromatin organization.

LADs are categorized into large chromatin regions that associate with the nuclear lamina in all cell types (constitutive, cLADs) and others that associate in a cell type-specific manner (facultative, fLADs)^{71,72}. The distribution of LADs determined by lamin A/C ChIP-seq analysis of HDFs was only minimally affected by AR silencing. There was increased binding of total and phospho-Ser301 lamin A/C to both hetero- and euchromatin regions without changes in their overall localization. Focusing on euchromatin changes of more direct relevance for CAF activation, we found a striking co-occurrence of increased phospho-Ser301 lamin A/C binding and peaks of open chromatin configuration and accessibility induced by AR silencing at the transcriptional promoter regulatory regions of the *TGFBRI* gene and other CAF effector genes. The findings are of likely functional significance as the expression of a phosphomimetic Ser/Asp 301 mutant resulted in expression of these genes as well as a wider transcriptional program of CAF activation related to the myofibroblast subtype^{10,73}. Strikingly, expression of the phosphomimetic mutant was by itself sufficient to confer upon HDFs the ability to enhance proliferation and tumorigenicity of neighboring cancer cells.

Nuclear lamin alterations have also been connected with genomic instability^{22,74}. While several studies reported chromosomal and gene copy number alterations in CAFs derived from breast, prostate, colorectal, and ovarian cancer⁷⁵⁻⁷⁸, the general view is that CAFs are “genetically stable”^{11,79}. This topic may need to be re-evaluated in the context of different organ and cancer types and exposure to various clastogenic agents. The skin—as the largest organ of the body with direct exposure to the environment—provides a unique system that allows careful analysis of CAFs and matched HDFs from flanking unaffected regions of the same patients. By previous comprehensive analysis, we demonstrated persistently elevated levels of DNA damage and telomeric instability in CAFs of skin SCCs versus matched HDFs⁸⁰, with a block of the downstream DNA damage response (DDR) by compensatory mechanisms that can involve specific genetic or epigenetic events⁸¹. Besides control of CAF gene transcription, it will be very interesting to determine to which extent the AR-lamin A/C interplay that we have uncovered bears also on genomic stability of these cells.

Previous studies on deregulated gene transcription resulting from nuclear lamin alterations in pathologic conditions implicated global changes in chromatin organization and looping as possible underlying mechanisms^{2,22}. In the case of CAF activation, we propose that the center stage is taken by more selective changes at the level of promoter regions of CAF effector genes, whereby phospho-Ser301 lamin A/C binding results in their increased expression. The close overlap with binding peaks of ATF3 and BRD4, two key regulators of CAF gene transcription⁸² point to an exciting interconnection to be explored in further studies in the context of actionable targets for stroma-focused anti-cancer intervention.



Methods

Study approvals

The research complies with all relevant ethical regulations and guidelines of the following institutional and competent authorities. All human samples were obtained from discarded tissue material collected from de-identified patients with written, informed consent. Discarded human foreskin samples were obtained from the Pediatric Surgery Department of the Lausanne University Hospital (department

de chirurgie pédiatrique of the Centre Hospitalier Universitaire Vaudois) with Human Ethics institutional review board approval and signed formularies of legally authorized representatives' consent (University of Lausanne; protocol # 222-12). Discarded skin tissue samples of squamous cell carcinoma (SCC) and flanking unaffected areas, from which CAFs and HDFs were derived, were obtained from the anonymized patients with institutional approval (2000P002418) at Massachusetts General Hospital (Boston, MA, USA). According to the

Fig. 5 | Lamin A/C phosphorylation at Ser 301 is a signature of CAFs. **A** IF analysis of CAFs and matched normal fibroblasts (HDFs) from the same patient showing phospho-Ser301 (pSer301) lamin A/C (red) and total lamin A/C (yellow). Representative images (left) and quantification of pSer301 lamin A/C fluorescence intensity (right), mean value as black bar. Two-tailed unpaired t-test, $n = 50$ cells per condition. Scale: $20 \mu\text{m}$. Similar analysis in Supplementary Fig. 5A. **B** CAFs treated with the AR agonist Ostarine ($10 \mu\text{M}$) or DMSO for 48 h. IF with antibodies against AR (green) and pSer301 lamin A/C (yellow). Representative images and quantification of pSer301 lamin A/C signal, mean value as black bar. Two-tailed unpaired t-test, $n = 51$ cells per condition. Scale: $20 \mu\text{m}$. **C** IF analysis of skin SCC-associated fibroblasts versus distal skin fibroblasts with antibodies against pSer301 lamin A/C (red), pan-cytokeratin (gray), and anti-PDGFR α (green). High magnification images shown, low magnification images are shown in Supplementary Fig. 5D. Scale: $5 \mu\text{m}$. **D** IF analysis of skin SCC-associated fibroblasts vs. distal skin fibroblasts with antibodies against pSer301 lamin A/C (red) and vimentin (gray). High magnification images shown, low magnification images are shown in Supplementary Fig. 5E. Scale: $5 \mu\text{m}$. **E** IF analysis of skin SCC-associated fibroblasts with antibodies against pSer301 lamin A/C (red), α -SMA (green), TNC (orange), and FAP (green; right). High

magnification images shown, low magnification images are shown in Supplementary Fig. 5F. Scale: $5 \mu\text{m}$. **F** Quantification of pSer301 in PDGFR α + and vimentin+ fibroblasts from SCC-associated vs. distal skin, and pSer301 in FAP, α -SMA, and TNC positive fibroblasts from SCC-associated regions, mean value as black bar. Two-tailed paired t-test, for PDGFR α + cells $n = 51$, vimentin+ cells $n = 47$ cells. **G** 3D volumetric surface reconstruction of confocal IF images of the SCC lesion and unaffected flanking skin as shown in Fig. 2E with antibodies against phospho-S301 (red) and total lamin A/C (yellow) and vimentin (purple), using the Imaris Surface tool, Manual mode. For each individual sample, threshold parameters were tested and set based on the weakest positive signal. **H** PLA of skin SCC-associated fibroblasts versus fibroblasts in distant unaffected skin with antibodies against lamin A/C and PPPICA/B (red puncta), with concomitant IF with anti-vimentin antibodies for cell type identification (green). Shown are representative images (left) and quantification (right) of PLA signal in vimentin-positive cells in matched pairs of skin SCC-associated versus distal skin fibroblasts from three different patients, with mean value as red bar. Two-tailed unpaired t-test, for patient-1, $n = 60$ cells; for patient-2, $n = 30$ cells, and for patient-3; $n = 37$ cells per condition. Scale: $30 \mu\text{m}$. Source data for individual graphs are in the Source Data file.

approved protocol for use of discarded human samples, they were de-identified and no clinical and personal information, including sex, was provided. Transcriptomic analysis of the three CAF strains and matched HDFs used for the present study indicated, on the basis of expression of Y chromosome genes, that they were from male patients. No compensation was provided to participants.

All animal studies were carried out according to Swiss guidelines for the use of laboratory animals, with protocols approved by the University of Lausanne animal care and use committee and the veterinary office of Canton Vaud (animal license No. 1854.4 e).

Cell culture

In this study, primary HDFs were extracted from the foreskin of young, healthy males aged 1–5 years, as described previously²⁰. Samples were obtained from the surgery department of the Centre Hospitalier Universitaire Vaudois (CHUV, Switzerland), with patient consent and institutional and approval (University of Lausanne; protocol # 222-12), no compensation was provided to participants. Briefly, 10 mg/mL Dispase (Merck, Cat# D4693-1G) was used to digest the tissue and separate the dermis from the epidermis. The epidermis was then digested using 1% collagenase (Merck, Cat# C9891) for 1 h at 37°C , followed by addition of the tissue extract was filtered through a $70 \mu\text{m}$ sieve, centrifuged, resuspended in complete medium and plated at a density of 1×10^5 cells/10 cm dish culture. The primary HDF strains used in this study, AK1, PB2 and AK2 were designated as HDF-1, HDF-2 and HDF-3 respectively. Please refer to the Supplementary Data S6 for a comprehensive list of all primary cells and cell lines used in this study.

Cancer-associated fibroblasts (CAFs) and matched normal fibroblasts (HDFs) were isolated from discarded skin tissue samples of squamous cell carcinoma (SCC) and flanking unaffected areas, respectively, obtained from the same (anonymized) patients with institutional approval (2000P002418) at Massachusetts General Hospital (Boston, MA, USA). Informed consent for research was obtained from the patients. The SCC and adjacent skin samples were provided as de-identified, discarded materials that were no longer needed for clinical use. No information regarding sex, gender, or patient identity was disclosed, and no compensation was provided to participants. Transcriptomic analysis of the three CAF strains and matched HDFs used for the present study indicated, on the basis of expression of Y chromosome genes, that they were from male patients. To isolate the fibroblasts, the clinical tissue sections were cut into small pieces ($1\text{--}2 \text{ mm}$) and incubated with 0.25 mg/mL Liberase TL (Roche, Cat# 05401020001) at 37°C for 40 min. After administration of FBS to stop the reaction, the tissues were filtered through a $70 \mu\text{m}$ sieve, centrifuged at $300 g$, resuspended in complete medium and plated at a density of 1×10^5 cells/10 cm dish culture.

Skin SCC13 tumor cell line was originally reported in ref. 83. For in vivo tumorigenesis assays, SCC13 cells were stably infected with an RFP-expressing lentivirus as previously described¹⁴.

HDFs, CAFs and SCC13 cells were maintained in Dulbecco's modified Eagle's medium (DMEM; Gibco, Cat# 31966021) supplemented with 10% fetal bovine serum (FBS; Gibco, Cat# 10270106) and 1% Penicillin-Streptomycin (BioConcept; Cat# 401F00H). Cells were cultured at 37°C and $5\% \text{ CO}_2$, and routine mycoplasma testing was performed. All experiments were conducted using cells from passages 4 to 10.

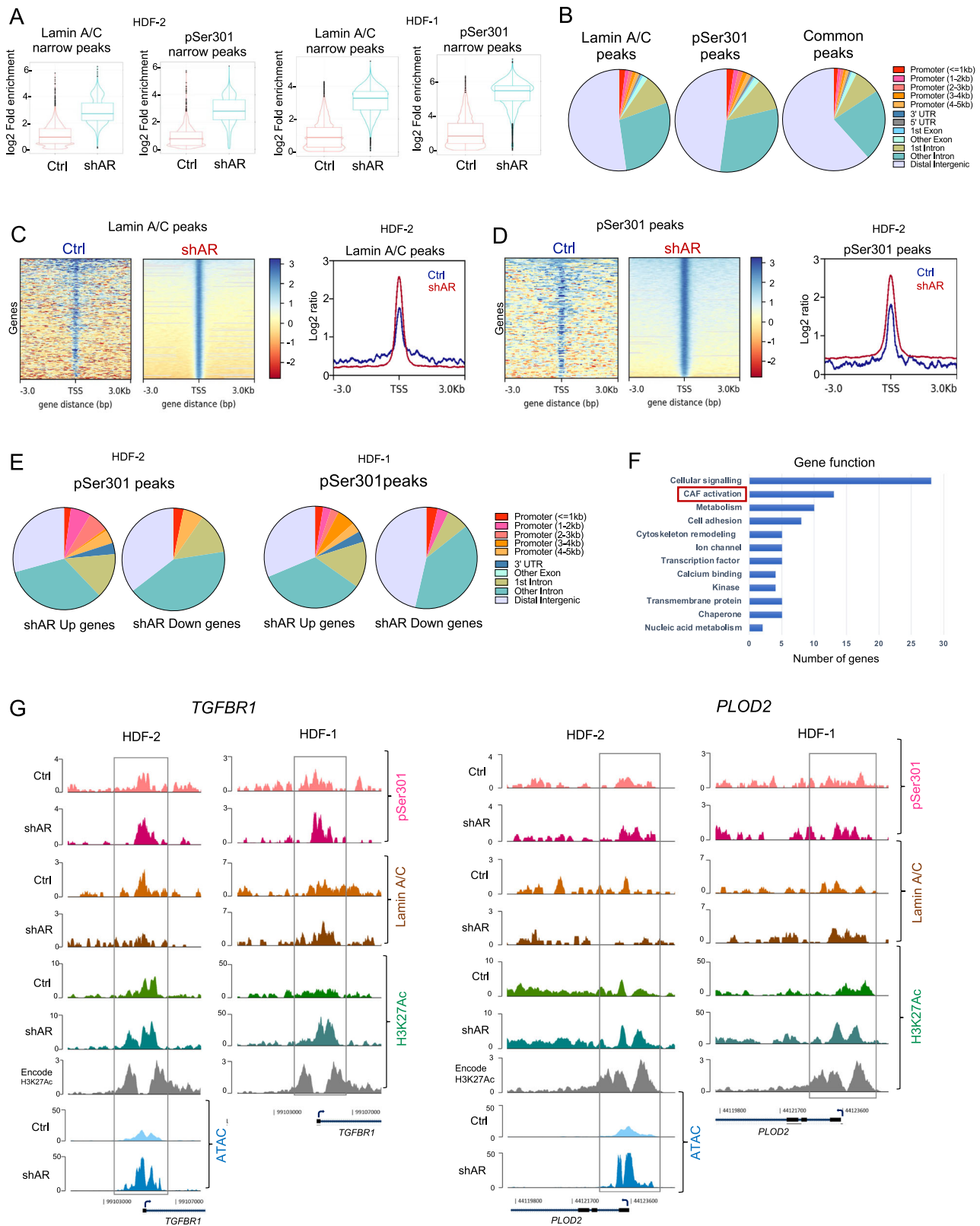
To culture cells on a soft matrix, HDFs were seeded onto collagen hydrogel-coated coverslips (Softslip; Cell Guidance Systems Ltd; Cat # SS24-COL-25) and allowed to grow for 48 h under standard culture conditions.

Cell manipulations

Short hairpin RNA (shRNA)-mediated silencing of androgen receptor (AR). Lentiviral particle production and AR silencing was performed following the previously described protocol¹⁶. Briefly, HDFs were transduced with lentiviruses expressing AR gene silencing shRNAs (shAR1 (TRCN000000003718) 5'-CACCAATGTCAACTCCAGGAT-3'; shAR2 (TRCN000000003715): 5'-CCTGCTAATCAAGTCACACAT-3', Sigma-Aldrich) in parallel with an empty pLko1 control vector (shCtrl; Sigma-Aldrich, Cat # NCLMIR001). The transduction was performed in DMEM medium supplemented with Polybrene ($0.8 \mu\text{g/mL}$) for a duration of 6 h. Two days after infection, HDFs were selected for puromycin resistance ($1 \mu\text{g/mL}$) and further analyzed 6 days post-infection. To bypass p53 dependent senescence, HDFs were stably infected with a TP53-silencing retrovirus followed by subsequent AR gene silencing using the protocol described before¹⁶.

AR overexpression. For the overexpression of AR, CAFs were stably infected with a blasticidin-resistant lentivirus that constitutively expresses AR (a gift from Karl-Henning Kalland, University of Bergen, Bergen, Norway) or with a lacZ control¹⁴. Two days post-infection, cells were selected for blasticidin resistance ($10 \mu\text{g/mL}$). AR- or lacZ-overexpressing cells were used for further analysis 6 days post-infection.

CRISPR/Cas9-mediated gene deletion. All-in-one lentiviral vectors encoding both the RNA guide (gRNA) and the Cas9 protein for AR gene deletion were obtained from Applied Biological Materials Inc. (Cat# 12233111). HDFs were infected with high-titer lentiviruses expressing two separate AR-targeting gRNAs (#1, #2) or a scrambled control guide RNA. After 48 h, cells were selected with puromycin ($1 \mu\text{g/mL}$), and the colonies were pooled before analysis of AR disruption. To further confirm the gene targeting efficiency, Surveyor assays were performed



one week after the infection. PCR was used to amplify the genomic regions encompassing the two targeted sequences for AR-gRNA. Subsequently, the amplified genomic DNA was then tested for the presence of a DNA-mismatch through incubation with a single-strand-specific endonuclease. The reactions of each targeted sequence were analyzed with a 2% agarose gel and compared to a similar reaction made with control gRNA-infected cells for specificity control.

Lamin A/C mutant expression. The Q5 Site-Directed Mutagenesis Kit (NEB, Cat# E0554S) was used to generate a Ser301 to Asp (S301D) mutant of lamin A/C from the wildtype lentiviral vector pCDH_blast_MCS_Nard_GFP_LAMIN (Addgene #167340)⁸⁴. Mutation-specific forward and reverse PCR primers, designed using NEBaseChanger tool (<https://nebasechanger.neb.com/>), were as follows: S301D Forward primer: 5' CCGCATCGACGACCTCTGCCCAG -3' and

Fig. 6 | AR is a determinant of chromatin association of total and phospho-Ser301 lamin A/C. **A** Box violin plots showing the enrichment of narrow peaks of total (Lamin A/C) and phospho-Ser301 (pSer301) lamin A/C binding to chromatin, as assessed by less stringent chromatin preparation followed by ChIP-seq analysis in two independent HDF strains (HDF-2, HDF-1) with shRNA-mediated *AR* silencing versus control. The box plots violin plots show enrichment of narrow peaks in each condition, with minimum, first quartile (lower bound), median, third quartile (upper bound), maximum values, whiskers up to 1.5 times the interquartile range. **B** The genomic distribution of unique and overlapping (within 500 bp of summits) peaks of total and phospho-Ser301 lamin A/C. Density heatmaps of the average distributions of total (**C**) and phospho-Ser301 lamin A/C (**D**) peaks around the TSS of genes (± 3 Kb) in control versus *AR* silenced (shAR) HDFs. The aggregation plots represent the enrichments peak signals in shAR (red line) versus control (blue line) conditions. **E** Genomic distribution of phospho-Ser301 peaks associated with genes

that are up or down-regulated in *AR* silenced HDFs. 10% of genes modulated by *AR* silencing was associated with pSer301 peaks with an overlap that by two-sided Chi-Square test was statistically significant (Supplementary Data S3). **F** Functional classification of shAR upregulated genes that were associated with pSer301 binding peaks in HDF-2. **G** Higher resolution genome browser view of phospho-Ser 301 and total lamin A/C binding peaks to the *TGFBR1* and *PLOD2* CAF effector genes in the HDF-2 and HDF-1 strains plus/minus *AR* gene silencing. ChIP-seq and ATAC-seq profiles were uploaded onto the EaSeq tool (<https://easeq.net/>). Position of the transcription start site (TSS) and part of the transcribed regions (solid lines) are indicated. The boxed area indicates the regulatory region of the gene around the TSS marked by experimentally determined H3K27Ac ChIP-seq profiles in parallel with those derived from the human dermal fibroblast profiles in ENCODE. Analysis of other genes of interest is provided in Supplementary Fig. 6D. Source data for relevant pie chart are in the Source Data file.

S301D Reverse primer: 5' ATGCGCAGTCTGCAGC -3'. The resulting mutant LMNA expressing construct (pCDH_blast_MCS_Nard_GFP_LAMIN_S301D) was confirmed by sequencing. The lentiviruses expressing either S301D or wildtype lamin A/C were used to transduce HDFs. Selection with blasticidin (10 μ g/ml) was used to create stable cell lines and, 6 days post-infection, the cells were analyzed using different assays.

Treatments. HDFs and CAFs were treated with different inhibitors or agonists in complete DMEM media containing 10% FBS and 1% antibiotics for a duration of 48–72 h as specified in figure legends. HDFs were treated with the *AR* inhibitor AZD3514 (10 μ M, Adooq Biosciences, Cat# A12396), the PPP1 inhibitor Tautomycin (10 μ M, Santa-Cruz, Cat# sc-507214) or DMSO as solvent control. CAFs were treated with the *AR* agonist Ostarine (Selleckchem, Cat# S1174) or DMSO. Furthermore, HDFs were cultured in DMEM supplemented with charcoal-treated FBS for 48 h prior to treatment with DHT (10 nM, Sigma-Aldrich, Cat# 10300), the *AR* degrading PROTAC ARCC4 (1 μ M, Tocris, Cat# 7254), or ethanol, and treatment was continued for the specified duration.

Proximity ligation assays

Proximity ligation assays (PLA) were performed using the Duolink[®] In Situ Red Kit Mouse/Rabbit (Sigma-Aldrich, Cat # DUO92101). For in vitro PLA, cells were cultured on 13-mm glass coverslips in 24-well plates for 24 h and fixed with 4% freshly prepared paraformaldehyde (PFA) for 10 min at room temperature (RT). Subsequently, cells were permeabilized with 0.1% Triton X-100 in PBS for 10 min at RT, followed by blocking with PLA blocking buffer in a humidified chamber at 37 °C for 2 h. The cells were then incubated overnight at 4 °C with the pairs of primary antibodies as indicated in the respective figure legends. The following day, tissue sections were washed three times with the kit-provided-buffers, and proximity ligation and rolling cycle probe amplification were performed following the manufacturer's protocol. Nuclei were counterstained with DAPI (1 μ g/ml; Merck, Cat# MBD0015).

For tissue PLA, freshly cut frozen tissue sections were fixed in 4% freshly prepared PFA for 10 min at RT. Tissue sections were then permeabilized with 0.5% Triton X-100 in PBS for 15 min at RT, blocked with PLA blocking buffer in a humidified chamber at 37 °C for 2 h, and incubated overnight at 4 °C with pairs of primary antibodies as indicated in figure legends. The following day, tissue sections were washed three times with the provided buffers, and proximity ligation and probe amplification were performed following the manufacturer's protocol. Tissue sections were additionally immunostained with A488-labeled anti-vimentin antibodies (Abcam, Cat# ab185030) and counterstained with DAPI. Details of all the different antibodies and dilutions used in PLA assays are indicated in the Supplementary Data S6.

Images were acquired using a Zeiss LSM 880 confocal microscope. The number of PLA puncta per cell was quantified using

ImageJ's Analyze Particle tool. Briefly, multi-color images were split into single channels and converted to grayscale. The threshold was adjusted to highlight structures of interest, and background pixels were subtracted. The "Watershed" option was used to separate merged nuclei. The binary image was then analyzed using the "Analyze Particles" function, with the settings adjusted to outline the nuclei. The same steps were repeated to analyze the image corresponding to PLA complexes. The outline images corresponding to nuclei and PLA complexes were inverted, resulting in an image where selected nuclei appeared in blue and PLA complexes in red. The PLA complexes outside the selected nuclei were excluded, and the average number of PLA puncta per cell was calculated.

Immunofluorescence

Frozen tissue sections or cultured cells on glass coverslips were fixed with cold 4% PFA for 15 min at RT. The fixed samples were washed with PBS and permeabilized with 0.1% Triton X-100 in PBS for 10 min, followed by incubation with 2% bovine serum albumin (BSA) in PBS for 2 h at RT. Primary antibodies were diluted in 2% BSA in PBS (pH 7.6) and incubated overnight at 4 °C. After washing three times in PBS, the samples were incubated with fluorescently labeled secondary antibodies (Invitrogen) for 1 h at RT. Following washing with PBS, slides were mounted with Fluoromount Mounting Medium (Sigma-Aldrich) after DAPI staining. Details of antibodies and dilutions used for immunostaining are indicated in the Supplementary Data S6.

Immunofluorescence images were acquired using a ZEISS LSM880 confocal microscope with 20 \times , 40 \times , or 63 \times objectives, and ZEN black software was used for image acquisition and processing. For fluorescence signal quantification, acquired images for each color channel were analyzed using ImageJ software, using the "measurement" or "particle analysis" functions to select areas or cells of interest (tumor or stromal). All measurements were exported as Microsoft Excel data files and data were plotted using GraphPad Prism 9.5.1 software. Imaris software v9 (Oxford Instruments) was used to create the 3D images. Z stack images acquired with Zeiss LSM880 confocal laser scanning microscope was utilized to recreate the volume at full resolution. The surface rendering method was used to create the 3D models. The surface area detail level (grain size) was set at 0.24 μ m, with an upper background subtraction of 0.904 μ m and a lower background subtraction threshold value of 10. The images were exported as TIFF.

Transmission electron microscopy (TEM)

The sample preparation and TEM analysis were carried out at the Electron Microscopy Facility at the University of Lausanne. Briefly, cells were grown on glass coverslips and fixed by incubating them with a fresh mixture of 2.5% glutaraldehyde (Sigma-Aldrich, Cat# G5882), 1% osmium tetroxide (EMS, Cat# 19110), and 1.5% potassium ferrocyanide (Sigma-Aldrich, Cat# 60279) in 0.1 M phosphate buffer (pH 7.4) for 1 h at room temperature. The samples were washed three times with

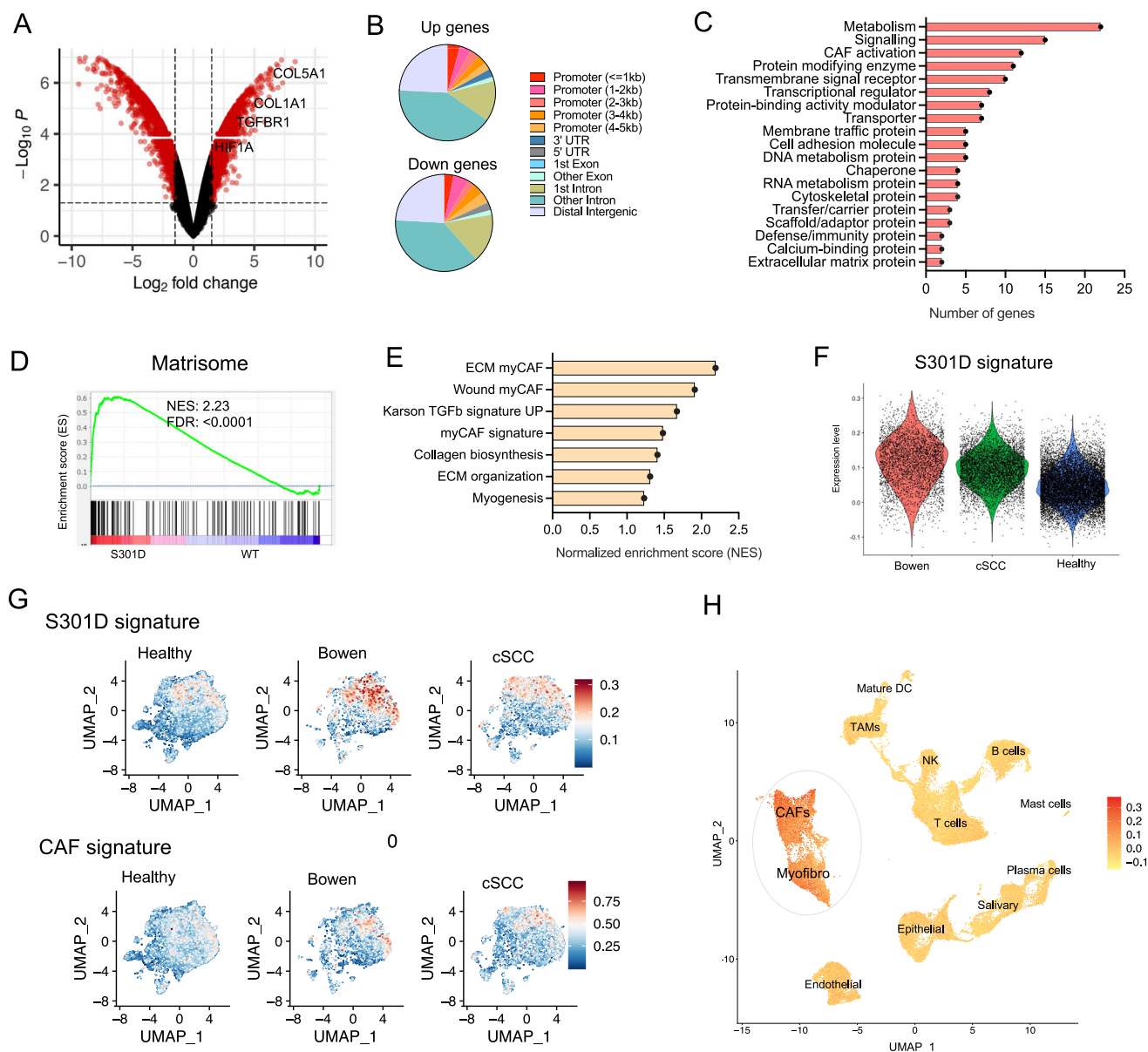


Fig. 7 | Expression of a phosphomimetic Ser 301 lamin A/C mutant induce CAF activation. **A** Volcano plot showing differentially expressed genes in HDFs expressing a phosphomimetic Ser to Asp 301 mutant (S301D) versus wild-type lamin A (WT). Transcriptomic Analysis Console software (TAC), p values were calculated by two-tailed unpaired t -test. Genes with fold changes >1.5 and p values <0.05 are highlighted in red. A few upregulated genes are indicated. A complete list of differentially expressed genes is in Supplementary Data S4. **B** Genomic Distribution of Phospho-Ser301 Peaks overlapping with genes up or downregulated in S301D-overexpressing HDFs. **C** Functional classification of common genes upregulated in both shAR HDFs and S301D-overexpressing cells were classified using Panther bioinformatics software and curated manually. **D** Gene Set Enrichment Analysis (GSEA) of transcriptomic profiles of HDFs expressing the S301D mutant versus WT lamin A. Positive enrichment plots of the CAF matrisome gene signature (GSE71340). Black vertical bars indicate the position of each gene; the enrichment plot is shown in green with normalized enrichment score (NES) and FDR- q values. **E** Bar plot indicating additional CAF-related pathways enriched in S301D-expressing HDFs. **F** Distribution of gene signature of 200 upregulated genes in S301D

expressing cells on fibroblasts derived from single-cell transcriptomic analysis of healthy skin, Bowen's disease or cutaneous SCC (cSCC)⁵⁵. **G** The Uniform Manifold Approximation and Projection (UMAP) of fibroblasts clusters of Bowen's disease and cutaneous SCC tumors⁵⁵ overlaid with the AddModule score of S301D signature (the top 200 upregulated genes in S301D expressing cells) and CAF signature⁹⁷. Each dot represents a single cell and color corresponds to the relative expression of the S301D signature within a cell. Blue corresponds to little/no gene expression, while red corresponds to increased gene expression as indicated in the scale. **H** Enrichment of the S301D lamin A/C gene signature on CAF and myofibroblast populations of head and neck squamous cell carcinoma (HNSCC) single cell clusters. Shown is the UMAP of different cell type clusters of HNSCC tumors⁵⁶ overlaid with the AddModule score of the top 200 upregulated genes in S301D expressing cells. Each dot represents a single cell and color corresponds to the relative expression of the S301D signature within a cell. Yellow corresponds to little/no gene expression, while red corresponds to increased gene expression as indicated in the scale. Source data for relevant graphs are in the Source Data file.

distilled water, and dehydration was performed by immersing the coverslips in 30% acetone for 5 min, followed by 50% acetone for 5 min. Subsequently, the coverslips were treated with a 0.3% uranyl acetate solution in 50% acetone for 20 min. The coverslip was then rinsed with

a 70% acetone solution in water for 5 min, and three sequential 5-min washes were performed using 100% acetone. A drop of 100% Epon resin was added to the coverslips and left overnight in a fume hood. The next morning, a gelatin capsule was completely filled with 100%

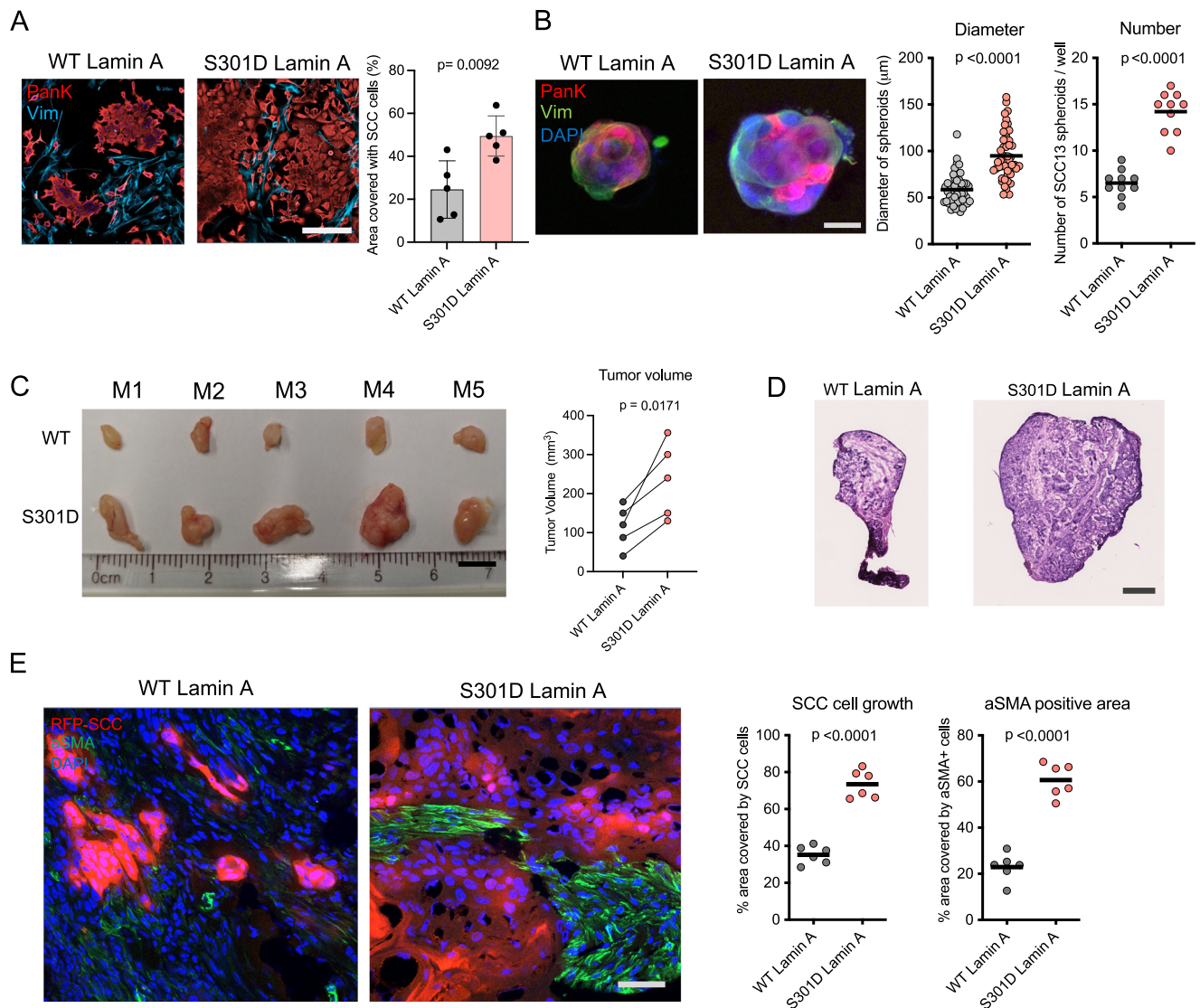


Fig. 8 | Expression of a phosphomimetic Ser 301 lamin A/C mutant is sufficient to trigger CAF phenotype and induce tumor growth.

A Cancer cells expansion assays. HDFs infected with lentiviruses expressing the S301D mutant versus wild-type (WT) lamin A were co-cultured with SCC13 cells on a thin matrigel layer for 4 days. Immunofluorescence analysis with anti-Pan-keratin (red) and -Vimentin (blue) antibodies was used for cell type identification. Percentage of SCC positive area was quantified by Image J analysis of 5 random fields per well. Two-tailed unpaired t-test, $n = 5$ independent replicate wells. Mean \pm SE. Scale: $100 \mu\text{m}$. **B** Spheroid formation assays. HDFs expressing the S301D mutant versus WT lamin A/C were co-cultured with SCC13 cells in 50% Matrigel-coated eight well glass slide for 7 days. IF with anti-Pan-keratin (red) and -Vimentin (green) antibodies were used for cell type identification. Shown are representative images and quantification of diameter and number of spheroids, mean value as black bar. Two-tailed unpaired

t-test, for diameter, $n = 25$ spheroids per condition; for spheroid numbers, $n = 10$ wells. Scale: $500 \mu\text{m}$. **C** *in vivo* tumor formation assays. RFP-expressing SCC13 cells were co-injected with HDFs expressing S301D mutant versus WT lamin A/C intradermally into contralateral mouse back skin. Mice were sacrificed 14 days later. Shown are images of excised xenograft tumor nodules and quantification of excised tumor volumes calculated using the formula $V = 3.14 \times (W^2 \times L)/6$ $V =$ volume, $W =$ width, and $L =$ length. Paired two-tailed t-test, $n = 5$ mice. Scale: 5 mm . **D** Representative H&E-stained images of the tumor lesions in (C). Scale bar: $500 \mu\text{m}$. **E** IF analysis of RFP-expressing SCC cells and α -SMA positive fibroblasts respectively. Shown are representative images and quantification of RFP and α -SMA-positive area per lesion, mean value as black bar. Two-tailed unpaired t-test, $n = 5$ tumors. Scale: $100 \mu\text{m}$. Source data for individual graphs are in the Source Data file.

Epon resin, turned over, and placed on the coverslip. The specimen was then polymerized at 60°C for 48 h. Ultrathin sections of 50 nm were cut on a Leica Ultracut (Leica) and transferred onto a copper slot grid ($2 \times 1 \text{ mm}$; EMS) coated with a polystyrene film. The sections were post-stained with 2% uranyl acetate (Sigma-Aldrich) in H_2O for 10 min, followed by rinsing with H_2O . Finally, the sections were stained with Reynolds's lead citrate (Sigma-Aldrich, Cat# 15326) in H_2O for 10 min and rinsed for a final time with H_2O . Micrographs were taken with a transmission electron microscope Philips CM100 (Thermo Fisher Scientific) at an acceleration voltage of 80 kV , using a TVIPS TemCam-F416 digital camera (TVIPS).

Cancer cells expansion assays

Cancer cell expansion assays were conducted as previously described¹⁶ with minor modifications. SCC13 tumor cells and fibroblasts were mixed in a 1:1 ratio in complete DMEM containing 1% Matrigel (BD Biosciences, Cat# 354230). Cells were plated on eight-well glass bottom culture slides (Corning, Cat# 354118), precoated with a thin layer of 10% Matrigel. Cells were allowed to grow for four days under normal culture conditions before fixing with 4% PFA. Immunofluorescence staining of HDFs and SCC13 cells were carried out with anti-vimentin and anti-pan-keratin antibodies and counterstained with fluorescently labeled secondary antibodies, as described above. Each well on the

slides was imaged using a Zeiss LSM880 confocal microscope with a 20× objective, and the percentage of SCC-positive area was quantified from five random fields per well using ImageJ software. The expansion of tumor cells was represented as a percentage of the SCC13 positive area.

3D spheroid assay

Eight-well glass bottom culture slides (Corning, Cat# 354118) were coated with 80% Matrigel (100 μ l per well; BD Biosciences, Cat# 354230) and incubated at 37 °C for 30 min to allow polymerization. RFP-expressing SCC13 cells and fibroblasts were mixed 1:1 in complete DMEM supplemented with 1% Matrigel and overlaid on wells containing polymerized 50% Matrigel. The spheroids were allowed to grow under normal culture conditions for six days. For immunostaining, the spheroids were fixed with 4% PFA and 2.5% glutaraldehyde for 10 min, carefully washed with PBS and stained with fluorescently labeled anti-*vimentin* antibody (Abcam, Cat# ab185030). Images of the spheroids were captured using a Zeiss LSM880 microscope with a 10× objective, and the diameter and number of spheroids were determined using ImageJ analysis.

Western blotting

Cells were lysed for 30 min on ice in lysis buffer (150 mM NaCl, 1.0% NP-40, 0.5% sodium deoxycholate, 0.1% SDS, 50 mM Tris, pH 8.0) containing a 1X protease/phosphatase inhibitor cocktail (Thermo Scientific, Cat# 78440). Protein concentration was then determined using a Pierce BCA protein detection kit (Thermo Scientific) and samples were normalized to 2 μ g/1 μ l. Proteins were then mixed with SDS-PAGE loading buffer (Tris pH 7.5 20 mM, EDTA 1 mM, SDS 1%) and boiled at 95 °C for 10 min. Proteins were then separated on 10–12% SDS-PAGE gels and transferred to a polyvinylidene difluoride membrane using the Trans-Blot Turbo™ transfer system (Bio-Rad). Membranes were blocked and primary antibodies were diluted in 2% BSA in Tris-buffered saline (TBS). The detection was performed by the use of peroxidase-conjugated secondary antibodies with the SuperSignal West Pico (Thermo Scientific). Signals were finally detected on Fuji Medical X-ray films (Fujifilm) or using iBright imaging systems (Invitrogen).

Time-lapse imaging and NERDI dynamics

GFP protein fused with a nuclear localization signal (GFP-NLS) was stably transduced into HDFs using lentiviruses (pTRIP-SFFV-EGFP-NLS; Addgene, Cat# 86677). Cells were cultured on eight-well coverslip-bottomed slides (ibidi GmbH, Cat# 80827), and imaged using a Zeiss Observer Z1 microscope equipped with a temperature- and CO₂-controlled stage-top incubation unit (Tokai Hit). Images were acquired at the indicated time intervals using an AxioCam MRM CCD camera (Zeiss) with a 20× objective. To minimize photodamage and phototoxicity, the illumination was set to 10% with an exposure time of 80 ms per slice.

For the analysis of nuclear envelope rupture during interphase (NERDI), time-lapse imaging was performed with 10-min intervals. The mean fluorescence intensity of GFP-NLS (BacMam, Thermo Fisher) within a defined region of the cell nucleus was quantified using ImageJ software. For data normalization, the peak fluorescence intensity of each sample was set to 1, and the lowest fluorescence intensity was set to 0. The data were aligned around the time point of NERDI and plotted using GraphPad Prism 9.5.1.

Co-immunoprecipitation

HDF cells were transduced with lentiviruses expressing either control or *AR*-targeting shRNA and selected with puromycin. After six days, cells were harvested and counted. Nuclear extracts were prepared from an equal number of control- or *AR* silenced cells using the NE-PER™ kit (Thermo Scientific, Cat# 78833), according to the

manufacturer's protocol. Briefly, the cell pellet was resuspended in ice-cold CER-I buffer containing a 1X protease/phosphatase inhibitor cocktail (Thermo Scientific, Cat# 78440). After vortexing for 15 s and incubating on ice for 10 min, the required volume of ice-cold CER II buffer was added. The pellet was vortexed for a further 5 s and centrifuged at maximum speed for 5 min. The supernatant containing the cytoplasmic extract was discarded and the pellet containing the nuclei was then lysed in ice-cold NER buffer containing a 1X protease/phosphatase inhibitor cocktail, vortexed for 15 s, and incubated on ice for 40 min with intermittent vortexing. The nuclear lysates were sonicated briefly with five pulses, and centrifuged at maximum speed for 10 min. The pellet containing chromatin and insoluble nuclear components was discarded, while the supernatant containing the nuclear extract was stored on ice, quantified and used for Co-IP. Equal amounts of nuclear lysates from control- and *AR* silenced cells were then diluted with Co-IP buffer (20 mM Tris-HCl pH = 8, 200 mM NaCl, 0.2% NP40, 2% glycerol, 0.05% sodium deoxycholate, 1.5 mM MgCl₂, 1X protease/phosphatase inhibitor cocktail) to a volume of 1 ml. The samples were then precleared with 10 μ l of Protein A Dynabeads (Invitrogen) and 1 μ l of DNase for 30 min at RT. Beads were removed and nuclear extracts were incubated overnight at 4 °C with either anti-lamin A/C antibody (Abcam, #ab108595) or non-immune IgG. The following day, pre-equilibrated Protein A Dynabeads were added, and the samples were incubated for at least 2 h at RT on a rotator. The supernatant was removed using magnetic separation, and the beads bound with the protein of interest were washed three times with 1 ml of 0.5X Co-IP buffer for 10 min at RT. Finally, the beads were washed with 1X PBS and subjected to mass spectrometry or immunoblot experiments.

Proteomics analysis

The proteomics analysis was performed at the Protein Analysis Facility of the University of Lausanne using the following methods.

SDS-PAGE and in-gel digestion. Co-IP samples were loaded onto a 12% mini polyacrylamide gel and migrated ~2–3 cm before being stained by Coomassie blue. Gel lanes between 10–300 kDa were excised into five-six pieces and subjected to in-gel digestion using sequencing-grade trypsin (Thermo Scientific, Cat# 90057), as previously described⁸⁵. The extracted tryptic peptides were then dried and resuspended in a 0.05% trifluoroacetic acid and 2% (v/v) acetonitrile solution.

Liquid chromatography-mass spectrometry analyses. Tryptic peptide mixtures were injected into a Dionex RSLC 3000 nanoHPLC system (Dionex, Sunnyvale, CA, USA), coupled with a high resolution QExact Plus mass spectrometer (Thermo Fisher) via a nanospray Flex source. Peptides were loaded onto a trapping microcolumn (Acclaim PepMap100 C18; 20 mm × 100 μ m ID, 5 μ m, Dionex) and separated on a custom-packed C18 column (75 μ m ID × 45 cm, 1.8 μ m particles). A gradient ranging from 4 to 76% acetonitrile in 0.1% formic acid for peptide separation (total time: 65 min). Full MS survey scans were performed at a resolution of 70,000. In data-dependent acquisition controlled by Xcalibur software (Thermo Fisher), the 10 most intense multiply charged precursor ions detected in the full MS survey scan were selected for higher energy collision-induced dissociation (HCD, normalized collision energy NCE = 27%) and analysis in the orbitrap at a 17,500 resolution. The window for precursor isolation was of 1.5 m/z units around the precursor and selected fragments were excluded for 60 s from further analysis.

Data processing. MS data were analyzed using Mascot 2.7.0 (Matrix Science, London, UK) with a search against the SwissProt database, restricted to the human (*Homo sapiens*) taxonomy (, version of June 2020, containing 20746 sequences), and a custom contaminant database containing common environmental contaminants and

digestion enzymes. Trypsin (cleavage at K,R) was used as the enzyme definition, allowing for up to two missed cleavages. Mascot searches were performed with a parent ion tolerance of 10 ppm and a fragment ion mass tolerance of 0.02 Da. Carbamidomethylation of cysteine was specified as a fixed modification, while protein N-terminal acetylation and methionine oxidation were specified as variable modifications.

Scaffold software (version Scaffold 4.11.1 or 5.0.0, Proteome Software Inc., Portland, OR) was used to validate MS/MS-based peptide and protein identifications by Mascot. Peptide identifications were accepted if they achieved a probability greater than 90.0% using either the Scaffold Local FDR algorithm (v. 4.11.1) or the Percolator posterior error probability calculation (v. 5.0.0)⁸⁶. Protein identifications were accepted if they had a probability greater than 95.0% and contained at least two identified peptides. Protein probabilities were determined using the Protein Prophet algorithm⁸⁷. Proteins that contained similar peptides and could not be differentiated based on MS/MS analysis alone were grouped to satisfy the principles of parsimony. Proteins sharing significant peptide evidence were grouped into clusters.

For the analysis of LMNA phosphorylation, the MS data from the corresponding gel bands were subjected to a secondary Mascot search, incorporating phosphorylation of serine, threonine and tyrosine as additional variable modifications. MsViz software⁸⁸ was used to compare intensities of phosphorylation sites between samples.

The mass spectrometry proteomics data generated in this study have been deposited to the ProteomeXchange Consortium via the PRIDE partner repository⁸⁹ with the dataset identifier PXD042059 and <https://doi.org/10.6019/PXD042059>.

Co-IP with recombinant proteins

In vitro protein interactions with recombinant proteins were performed as follows. 200 ng purified Myc-tagged lamin A (MW: 74 kDa, OriGene; Cat# TP304970) and 200 ng 6XHis-tagged AR-NTD (1-556 aa, 63 kDa, Ray Biotech; Cat# RB-14-0003P) were mixed in 500 μ l binding buffer (150 mM NaCl, 20mM Tris-HCl; pH-8, 0.1% NP40, 10% glycerol) and incubated overnight at 4 °C on a rotary platform. The next day, 20 μ l of protein A magnetic beads pre-adsorbed with 0.5 μ g of anti-lamin A/C antibody (Abcam, #ab108595) were added to the protein mixture and incubated for 2 h at RT. Bead-bound protein complexes were separated from the unbound fraction by magnetic pull-down, beads were washed three times in binding buffer and then resuspended in 30 μ l of SDS-PAGE loading buffer. As a control for specificity, parallel pull-down reactions were performed with AR protein previously denatured by a short heat treatment (20 min at 85 °C), or the protein mixture was incubated in high salt buffer (800 mM NaCl). Immunoprecipitates with anti-lamin A/C antibody were analyzed in parallel with 5% unbound supernatants by immunoblotting with anti-lamin A/C (Cell Signaling; Cat# #4777) or anti-His (Cell Signaling; Cat#12698) antibodies. Additional co-IPs were carried out with individual domains of Lamin A and AR proteins. Myc-tagged Lamin A full length or His-tagged Lamin A -rod domain (1-422 aa; 53 kDa, LS Bio; Cat# LS-G25618) were mixed with AR-NTD or AR ligand-binding C-terminal domain (LBD; aa. 699-920) in binding buffer and immunoprecipitation were carried out with anti-lamin A/C antibody as described above. The Immunoprecipitates were analyzed in parallel with individual protein inputs using HRP conjugated anti-myc (Abcam; ab62928) or anti-His (Abcam; Cat# ab1187) or anti AR-CTD (Cell Signaling; Cat #54653) antibodies.

ChIP-seq

Control- and AR-silenced fibroblasts were cross-linked with 1% formaldehyde for 10 min at RT, followed by quenching with glycine (final concentration 125 mM). After washing with ice-cold PBS, cells were collected through centrifugation (400 g). For the analysis of total lamin A/C chromatin binding, cells were lysed, and chromatin was prepared using the Chromatin EasyShear Kit - High SDS (Diagenode;

Cat# C01020012) and shearing of the chromatin was achieved using the Bioruptor with four rounds of ten cycles of 30 s “ON” and 30 s “OFF” at HIGH power setting (position H). To determine chromatin binding of phospho-Ser301 and wild-type lamin A/C together with histone markers, chromatin was prepared using the Chromatin EasyShear Kit - Low SDS (Diagenode, Cat# C01020013) and sonicated using an E220 focused ultrasonicator (Covaris).

The ChIP reaction was performed using the iDeal ChIP-seq kit (Diagenode, Cat# C01010055). Samples were pre-cleared using the beads provided in the kit and incubated overnight at 4 °C with 5 μ g of commercially available antibodies against lamin A/C (Abcam, #ab108595), phospho-Ser301 lamin A/C (Affinity, #AF7177), H3K27Ac (Abcam, #ab4729). Antibody-chromatin complexes were pulled down using protein A-coated magnetic beads. Elution was performed according to the manufacturer's instruction and chromatin was quantified using the Qubit Fluorometric Quantification Kit (Thermo Scientific). For library preparation, 10 ng of DNA was utilized with the NEBNext® ChIP-Seq Library Prep Reagent Set for Illumina. Subsequently, pair-end sequencing was performed at the Novogene facility using the Novaseq 6000 platform.

The FASTA files were aligned using the Burrows-Wheeler Aligner (BWA)⁹⁰ and narrow peaks were detected using MACS2 software⁹¹ with a *q* value cut-off of 0.05. Graphic illustrations of ChIP-seq peaks were generated using the Easeq tool, an interactive software for analysis and visualization of ChIP-sequencing data (<https://easeq.net/>). Peaks were annotated and merged using the annotatePeaks.pl and mergepeaks.pl functions available in the HOMER software⁹².

To detect lamin A/C associated with LADs, we used the EDD, a tool developed to analyze broad enrichment domains from ChIP-seq data⁴⁵. Mapped reads from BAM files were used to call LADs, with automatic estimation of GapPenalty. Log ratios between input and ChIP samples were calculated using a BinSize of 10 Kb, with the human genome hg38 as the reference assembly. Peaks were retrieved with an FDR *p*-value of 0.05.

ChIP-seq datasets generated for this study were deposited in the NCBI Gene Expression Omnibus (GEO) with accession number GSE230507 and GSE273342.

ChIP-PCR

The chromatin sharing of shAR and control HDFs were carried out using Chromatin EasyShear - Low SDS kit and ChIP experiments were performed as described above using two different anti-phospho-Ser301 lamin A/C antibodies (Affinity, Cat#AF7177 and Thermo; cat# PA5-105449, respectively). 1 μ l of eluted ChIP samples was used as a template for qPCR to determine the enrichment on the promoter regions of indicated genes. Additionally, ChIP-PCR experiments were carried out in HDFs overexpressing GFP-tagged wildtype or S301D mutant lamin A. These experiments employed an anti-GFP antibody (Abcam; Cat#ab290) and followed the aforementioned protocol. The ChIP-PCR primer sequences are listed in Supplementary Data S6.

ATAC-seq

ATAC-seq analysis was conducted on the same batch of AR-silenced and control HDFs that were used for ChIP-seq analysis. Viable cells were harvested, and their viability was assessed using the trypan blue assay and cell counting. ATAC-seq was performed as previously reported⁹³⁻⁹⁵. Briefly, nuclei were extracted from 50,000 cells and the nuclear pellet was resuspended in the Tn5 transposase reaction mix (Diagenode, Cat# C01070012-30). The transposition reaction was incubated at 37 °C for 30 min. Afterward, DNA fragments were purified and isolated using the MinElute Reaction Cleanup Kit (Qiagen, Cat # 28204). The purified DNA fragments were quantified using Qubit, and library preparation was performed. ATAC-seq library preparation involved PCR amplification of the purified DNA fragments using Diagenode primer indices (Diagenode, Cat# C01011034).

Amplification cycles were adjusted and libraries were purified using AMPure beads. Library quality was assessed using Qubit and Bioanalyzer, and the final libraries were sequenced on an Illumina Novaseq 6000 machine.

For ATAC-seq data analysis, raw data underwent quality control using FastQC. Trimming and filtering were performed, which included the removal of adapter sequences, low-quality reads (average quality score below 20, an N ratio exceeding 15%, adapters, or a length of less than 18 nucleotides after trimming) and trimming of adapter sequences at the 3' end. The reads were then aligned to the human reference genome (GRCh38/hg38) using BWA⁹⁰. Following alignment, peaks were called using the MACS2 algorithm (<http://liulab.dfci.harvard.edu/MACS>). To analyze the distribution of peaks across different functional domains, ChIPseeker software⁹⁶ was used.

The ATAC-seq datasets generated for this study were deposited in the NCBI GEO under accession number GSE230416.

Cut & Run

Cut & Run assays were performed using the CUTANA™ ChIC/CUT&RUN Kit (EpiCypher; Cat. No. # SKU: 14-1048) to investigate chromatin interactions of phospho-Ser301 and total Lamin A/C in parallel to H3K27Ac in HDF cells with and without AR silencing. Cells were cultured, harvested, and processed following the kit protocol. Briefly, 500,000 cells were incubated with Protein A-MNase fusion protein, digested with Micrococcal Nuclease, and nuclei were washed and incubated with Protein A-G-MNase beads for elution. DNA purification and library preparation were performed, followed by Illumina sequencing. Data analysis involved alignment, peak calling, and differential binding analysis using bioinformatics tools, with BWA-MEM and Macs2 for peak calling, with $p = 0.001$. Raw and processed data were deposited in a public repository for accessibility and further research: GSE266428.

Transcriptomic analysis

Two HDF strains were stably infected with lentiviruses expressing S301D or wild-type lamin A (WT). Eight days post-infection, transcriptomic analysis was performed using Clariom D cDNA array hybridization. RNA extraction and purification was carried out using the Direct-zol RNA Miniprep Kit (Zymo Research). The quality of RNA samples was assessed, ensuring a purity of OD260/OD280 ≥ 1.8 and RIN ≥ 8 . Global transcriptomic analysis was conducted at the Institute of Genetics and Genomics of Geneva (iGE3) using Clariom™ D GeneChip assays. Briefly, the GeneChip® WT PLUS Reagent Kit (Thermo Fisher Scientific, Cat. No. 902280) was used to prepare samples and to facilitate hybridization to the human Clariom™ D arrays (Thermo Fisher Scientific). Transcriptome Analysis Console (TAC) software (Thermo Fisher Scientific) was used for data processing and analysis. The data generated in this study have been deposited in the publicly accessible functional genomics data repository GEO, under accession number GSE233200.

GSEA for Clariom D array expression profiles was performed as in¹⁶ by using GSAA-SeqSP software (gene set association analysis for array expression data with sample permutation) from the Gene Set Association Analysis (GSAA) platform (version GSAA 2.0, Signatures were downloaded from the GSEA web page (<http://www.gsea-msigdb.org/gsea/msigdb/human/genesets.jsp>). Curated gene sets were obtained from the Molecular Signatures Database (MSigDB v5.2; <http://www.broadinstitute.org/gsea/msigdb/>) or from the GEO database with respective accession numbers as indicated, and the TGF- β signature (GSE79621), CAF gene signature (GSE122372) and myCAF (GSE93313) was downloaded from respective GEO.

Normalized single-cell RNA-seq profiles generated from cutaneous squamous cell carcinoma (sSCC, Bowen's disease) and HNSCC samples using the 10X Genomics platform were downloaded from Gene Expression Omnibus (GSE218170⁵⁵ and GSE188737⁵⁶). Scaling and

dimensionality reduction with PCA and UMAP were performed using Seurat v4.3.0 (www.satijalab.org/seurat). The top 200 up-regulated genes from the Lamin A/C S301D transcriptomic data were used to calculate signature scores using the Seurat function 'AddModuleScore' 75. All analyses were performed in R v4.2.1.

RT-qPCR analysis was performed as described previously¹⁶. A list of primers used in this study is provided in the Supplementary Data S6.

Tumorigenesis experiments

Animal experiments were completed in accordance with the Swiss guidelines and regulations for the care and use of laboratory animals with approved protocol from the Canton de Vaud veterinary office (animal license No. 1854.4e). All mice were housed in the animal facility of the University of Lausanne. Mice were housed in five per cage on a 12-h dark/light cycle, with a constant ambient temperature of 65–70 F and 40% humidity. All the mice were randomly allocated to the experimental groups and group-housed. Throughout the study, humane endpoints were implemented to ensure the well-being of the mice.

Mouse back injections were carried out in 9-week-old NOD/SCID male mice (with IL-2 receptor γ chain null mutation, *NOD.Cg-Prkdcscid Il2rytm1Wjl/Szj*, (the Jackson Laboratory). 2.5×10^5 RFP-SCC13 tumor cells, admixed with an equal number of HDFs expressing either S301D mutant or wildtype lamin A/C were re-suspended in 70 μ l of Matrigel solution (BD Bioscience) and injected intradermally into the left and right side of the mouse back. Mice were sacrificed for tissue analysis 14 days after injection. The tumor volumes were calculated using the formula $V = 3.14 \times (W^2 \times L)/6$ V = volume, W = width, and L = length. The maximal tumor size permitted by the approved protocol was 20 mm in any direction, which was not exceeded in any experiment. All mice were euthanized by carbon dioxide inhalation. No animal died or was excluded from the experiments.

Statistics and reproducibility

Statistical testing is performed using GraphPad Prism 9.5.1 and Prism 10 Software. Data are presented as mean \pm SE, as indicated in the legend. For each experiment, two to three separated cell strains were used in independent experiments. Statistical significance for comparing two experimental conditions is calculated by two-tailed unpaired or paired t-tests, while for comparing one control with two experimental conditions the statistical significance is calculated using the nonparametric one-way ANOVA test. All p values < 0.05 are considered statistically significant and p values are indicated in the respective figures.

Reporting summary

Further information on research design is available in the Nature Portfolio Reporting Summary linked to this article.

Data availability

Source data are provided with this paper. The transcriptomic, ChIP-seq, ATAC and Cut & Run data (raw and processed datasets) generated in this study are available under the GEO repository with the following IDs. Transcriptomics data with GEO accession GSE233200: ChIP-seq analysis data with GEO accession GSE230507; and GSE273342: ATAC-seq analysis data with GEO accession GSE230416: Cut & Run analysis data with GEO accession GSE266428: The Mass Spectroscopy dataset has been submitted to ProteomeXchange Consortium with Project accession: PXD042059 and Project <https://doi.org/10.6019/PXD042059>. Source data are provided with this paper.

References

1. Denais, C. & Lammerding, J. Nuclear mechanics in cancer. *Adv. Exp. Med. Biol.* **773**, 435–470 (2014).

2. Karoutas, A. & Akhtar, A. Functional mechanisms and abnormalities of the nuclear lamina. *Nat. Cell Biol.* **23**, 116–126 (2021).
3. Uhler, C. & Shivashankar, G. V. Nuclear mechanopathology and cancer diagnosis. *Trends Cancer* **4**, 320–331 (2018).
4. Biffi, G. & Tuveson, D. A. Diversity and biology of cancer-associated fibroblasts. *Physiol. Rev.* **101**, 147–176 (2021).
5. Chen, Y., McAndrews, K. M. & Kalluri, R. Clinical and therapeutic relevance of cancer-associated fibroblasts. *Nat. Rev. Clin. Oncol.* **18**, 792–804 (2021).
6. Davidson, S. et al. Fibroblasts as immune regulators in infection, inflammation and cancer. *Nat. Rev. Immunol.* **21**, 704–717 (2021).
7. Gascard, P. & Tlsty, T. D. Carcinoma-associated fibroblasts: orchestrating the composition of malignancy. *Genes Dev.* **30**, 1002–1019 (2016).
8. Hiebert, P. et al. Nrf2-mediated fibroblast reprogramming drives cellular senescence by targeting the matrisome. *Dev. Cell* **46**, 145–161.e10 (2018).
9. Kalluri, R. The biology and function of fibroblasts in cancer. *Nat. Rev. Cancer* **16**, 582–598 (2016).
10. Lavie, D., Ben-Shmuel, A., Erez, N. & Scherz-Shouval, R. Cancer-associated fibroblasts in the single-cell era. *Nat. Cancer* **3**, 793–807 (2022).
11. Sahai, E. et al. A framework for advancing our understanding of cancer-associated fibroblasts. *Nat. Rev. Cancer* **20**, 174–186 (2020).
12. Campisi, J., Andersen, J. K., Kapahi, P. & Melov, S. Cellular senescence: a link between cancer and age-related degenerative disease? *Semin. Cancer Biol.* **21**, 354–359 (2011).
13. Goruppi, S. & Dotto, G. P. Mesenchymal stroma: primary determinant and therapeutic target for epithelial cancer. *Trends Cell Biol.* **23**, 593–602 (2013).
14. Ma, M. et al. Sustained androgen receptor signaling is a determinant of melanoma cell growth potential and tumorigenesis. *J. Exp. Med.* **218**, e20201137 (2021).
15. Samarkina, A. et al. Androgen receptor is a determinant of melanoma targeted drug resistance. bioRxiv. <https://doi.org/10.1101/2022.05.27.493720> (2022).
16. Clocchiatti, A. et al. Androgen receptor functions as transcriptional repressor of cancer-associated fibroblast activation. *J. Clin. Invest.* **128**, 5531–5548 (2018).
17. Mazzeo, L. et al. ANKRD1 is a mesenchymal-specific driver of cancer-associated fibroblast activation, bridging androgen receptor loss to AP-1 activation. *Nat. Commun.* **15**, 1038 (2024).
18. Faget, D. V., Ren, Q. & Stewart, S. A. Unmasking senescence: context-dependent effects of SASP in cancer. *Nat. Rev. Cancer* **19**, 439–453 (2019).
19. Krtolica, A., Parrinello, S., Lockett, S., Desprez, P. Y. & Campisi, J. Senescent fibroblasts promote epithelial cell growth and tumorigenesis: a link between cancer and aging. *Proc. Natl. Acad. Sci. USA* **98**, 12072–12077 (2001).
20. Procopio, M. G. et al. Combined CSL and p53 downregulation promotes cancer-associated fibroblast activation. *Nat. Cell Biol.* **17**, 1193–1204 (2015).
21. Erez, N., Truitt, M., Olson, P., Arron, S. T. & Hanahan, D. Cancer-associated fibroblasts are activated in incipient neoplasia to orchestrate tumor-promoting inflammation in an NF- κ B-dependent manner. *Cancer Cell* **17**, 135–147 (2010).
22. de Leeuw, R., Gruenbaum, Y. & Medalia, O. Nuclear lamins: thin filaments with major functions. *Trends Cell Biol.* **28**, 34–45 (2018).
23. Dittmer, T. A. & Misteli, T. The lamin protein family. *Genome Biol.* **12**, 222 (2011).
24. Gruenbaum, Y. & Foisner, R. Lamins: nuclear intermediate filament proteins with fundamental functions in nuclear mechanics and genome regulation. *Annu. Rev. Biochem.* **84**, 131–164 (2015).
25. Kubben, N., Voncken, J. W. & Misteli, T. Mapping of protein- and chromatin-interactions at the nuclear lamina. *Nucleus* **1**, 460–471 (2010).
26. Tatli, M. & Medalia, O. Insight into the functional organization of nuclear lamins in health and disease. *Curr. Opin. Cell Biol.* **54**, 72–79 (2018).
27. Doudna, J. A. & Charpentier, E. The new frontier of genome engineering with CRISPR-Cas9. *Science* **346**, 1258096 (2014).
28. Qiu, P. et al. Mutation detection using Surveyor nuclease. *Bio-techniques* **36**, 702–707 (2004).
29. Salami, J. et al. Androgen receptor degradation by the proteolysis-targeting chimera ARCC-4 outperforms enzalutamide in cellular models of prostate cancer drug resistance. *Commun. Biol.* **1**, 100 (2018).
30. Loddick, S. A. et al. AZD3514: a small molecule that modulates androgen receptor signaling and function in vitro and in vivo. *Mol. Cancer Ther.* **12**, 1715–1727 (2013).
31. Vargas, J. D., Hatch, E. M., Anderson, D. J. & Hetzer, M. W. Transient nuclear envelope rupturing during interphase in human cancer cells. *Nucleus* **3**, 88–100 (2012).
32. Matsumoto, T. et al. The androgen receptor in health and disease. *Annu. Rev. Physiol.* **75**, 201–224 (2013).
33. Narayanan, R., Coss, C. C. & Dalton, J. T. Development of selective androgen receptor modulators (SARMs). *Mol. Cell Endocrinol.* **465**, 134–142 (2018).
34. Liu, S. Y. & Ikegami, K. Nuclear lamin phosphorylation: an emerging role in gene regulation and pathogenesis of laminopathies. *Nucleus* **11**, 299–314 (2020).
35. Zheng, X. et al. Lamins organize the global three-dimensional genome from the nuclear periphery. *Mol. Cell* **71**, 802–815.e7 (2018).
36. Dittmer, T. A. et al. Systematic identification of pathological lamin A interactors. *Mol. Biol. Cell* **25**, 1493–1510 (2014).
37. Wilson, K. L. & Foisner, R. Lamin-binding proteins. *Cold Spring Harb. Perspect. Biol.* **2**, a000554 (2010).
38. Thompson, L. J., Bollen, M. & Fields, A. P. Identification of protein phosphatase 1 as a mitotic lamin phosphatase. *J. Biol. Chem.* **272**, 29693–29697 (1997).
39. Chen, S., Kesler, C. T., Paschal, B. M. & Balk, S. P. Androgen receptor phosphorylation and activity are regulated by an association with protein phosphatase 1. *J. Biol. Chem.* **284**, 25576–25584 (2009).
40. Huguet, F., Flynn, S. & Vagnarelli, P. The role of phosphatases in nuclear envelope disassembly and reassembly and their relevance to pathologies. *Cells* **8**, 687 (2019).
41. Zheng, M., Jin, G. & Zhou, Z. Post-translational modification of lamins: mechanisms and functions. *Front. Cell Dev. Biol.* **10**, 864191 (2022).
42. Mitsuhashi, S. et al. Tautomycin is a novel and specific inhibitor of serine/threonine protein phosphatase type 1, PP1. *Biochem. Biophys. Res. Commun.* **287**, 328–331 (2001).
43. van Steensel, B. & Belmont, A. S. Lamina-associated domains: links with chromosome architecture, heterochromatin, and gene repression. *Cell* **169**, 780–791 (2017).
44. Ikegami, K., Secchia, S., Almakki, O., Lieb, J. D. & Moskowitz, I. P. Phosphorylated lamin A/C in the nuclear interior binds active enhancers associated with abnormal transcription in progeria. *Dev. Cell* **52**, 699–713.e11 (2020).
45. Lund, E., Oldenburg, A. R. & Collas, P. Enriched domain detector: a program for detection of wide genomic enrichment domains robust against local variations. *Nucleic Acids Res.* **42**, e92 (2014).
46. Lund, E. G., Duband-Goulet, I., Oldenburg, A., Buendia, B. & Collas, P. Distinct features of lamin A-interacting chromatin domains mapped by ChIP-sequencing from sonicated or micrococcal nuclease-digested chromatin. *Nucleus* **6**, 30–39 (2015).

47. Wu, D.-Y., Bittencourt, D., Stallcup, M. R. & Siegmund, K. D. Identifying differential transcription factor binding in ChIP-seq. *Front. Genet.* **6**, 169 (2015).
48. Bordignon, P. et al. Dualism of FGF and TGF- β signaling in heterogeneous cancer-associated fibroblast activation with ETV1 as a critical determinant. *Cell Rep.* **28**, 2358–2372.e6 (2019).
49. Prakash, K. & Fournier, D. Histone code and higher-order chromatin folding: a hypothesis. *Genom. Comput. Biol.* **3**, e41 (2017).
50. Winkler, J. et al. Concepts of extracellular matrix remodelling in tumour progression and metastasis. *Nat. Commun.* **11**, 5120 (2020).
51. Kennel, K. B. et al. Cancer-Associated Fibroblasts in Inflammation and Antitumor Immunity. *Clin. Cancer Res.* **29**, 1009–1016 (2023).
52. Kay, E. J. et al. Cancer-associated fibroblasts require proline synthesis by PYCR1 for the deposition of pro-tumorigenic extracellular matrix. *Nat. Metab.* **4**, 693–710 (2022).
53. Meers, M. P., Bryson, T. D., Henikoff, J. G. & Henikoff, S. Improved CUT&RUN chromatin profiling tools. *eLife* **8**, e46314 (2019).
54. Lambrechts, D. et al. Phenotype molding of stromal cells in the lung tumor microenvironment. *Nat. Med.* **24**, 1277–1289 (2018).
55. Schütz, S. et al. Functionally distinct cancer-associated fibroblast subpopulations establish a tumor promoting environment in squamous cell carcinoma. *Nat. Commun.* **14**, 5413 (2023).
56. Quah, H. S. et al. Single cell analysis in head and neck cancer reveals potential immune evasion mechanisms during early metastasis. *Nat. Commun.* **14**, 1680 (2023).
57. Caligiuri, G. & Tuveson, D. A. Activated fibroblasts in cancer: perspectives and challenges. *Cancer Cell* **41**, 434–449 (2023).
58. Watson, P. A., Arora, V. K. & Sawyers, C. L. Emerging mechanisms of resistance to androgen receptor inhibitors in prostate cancer. *Nat. Rev. Cancer* **15**, 701–711 (2015).
59. Shiota, M., Yokomizo, A. & Naito, S. Increased androgen receptor transcription: a cause of castration-resistant prostate cancer and a possible therapeutic target. *J. Mol. Endocrinol.* **47**, R25–R41 (2011).
60. Samarkina, A. et al. Androgen receptor is a determinant of melanoma targeted drug resistance. *Nat. Commun.* **14**, 6498 (2023).
61. Robert, M. & Crasta, K. Breaking the vicious circle: extra-chromosomal circular DNA as an emerging player in tumour evolution. *Semin. Cell Dev. Biol.* **123**, 140–150 (2022).
62. de Las Heras, J. I., Batrakou, D. G. & Schirmer, E. C. Cancer biology and the nuclear envelope: a convoluted relationship. *Semin Cancer Biol.* **23**, 125–137 (2013).
63. Bachelor, M. A. & Bowden, G. T. UVA-mediated activation of signaling pathways involved in skin tumor promotion and progression. *Semin. Cancer Biol.* **14**, 131–138 (2004).
64. Jolly, C. & Morimoto, R. I. Stress and the cell nucleus: dynamics of gene expression and structural reorganization. *Gene Expr.* **7**, 261–270 (1999).
65. Dobs, A. S. et al. Effects of enobosarm on muscle wasting and physical function in patients with cancer: a double-blind, randomised controlled phase 2 trial. *Lancet Oncol.* **14**, 335–345 (2013).
66. Roch, P. J. et al. Ostarine and ligandrol improve muscle tissue in an ovariectomized rat model. *Front. Endocrinol.* **11**, 556581 (2020).
67. Dozmorov, M. G. et al. Unique patterns of molecular profiling between human prostate cancer LNCaP and PC-3 cells. *Prostate* **69**, 1077–1090 (2009).
68. Nilsson, J. Protein phosphatases in the regulation of mitosis. *J. Cell Biol.* **218**, 395–409 (2019).
69. Cohen, P. T. Protein phosphatase 1-targeted in many directions. *J. Cell Sci.* **115**, 241–256 (2002).
70. Bertacchini, J. et al. The protein kinase Akt/PKB regulates both prelamins A degradation and Lmna gene expression. *FASEB J.* **27**, 2145–2155 (2013).
71. Kind, J. et al. Genome-wide maps of nuclear lamina interactions in single human cells. *Cell* **163**, 134–147 (2015).
72. Peric-Hupkes, D. et al. Molecular maps of the reorganization of genome-nuclear lamina interactions during differentiation. *Mol. Cell* **38**, 603–613 (2010).
73. Ohlund, D., Elyada, E. & Tuveson, D. Fibroblast heterogeneity in the cancer wound. *J. Exp. Med.* **211**, 1503–1523 (2014).
74. Gonzalez-Suarez, I. et al. Novel roles for A-type lamins in telomere biology and the DNA damage response pathway. *EMBO J.* **28**, 2414–2427 (2009).
75. Tuhkanen, H. et al. Frequent gene dosage alterations in stromal cells of epithelial ovarian carcinomas. *Int. J. Cancer* **119**, 1345–1353 (2006).
76. Pelham, R. J. et al. Identification of alterations in DNA copy number in host stromal cells during tumor progression. *Proc. Natl. Acad. Sci. USA* **103**, 19848–19853 (2006).
77. Rummel, S., Valente, A. L., Kane, J. L., Shriver, C. D. & Ellsworth, R. E. Genomic (in)stability of the breast tumor microenvironment. *Mol. Cancer Res.* **10**, 1526–1531 (2012).
78. Allinen, M. et al. Molecular characterization of the tumor microenvironment in breast cancer. *Cancer Cell* **6**, 17–32 (2004).
79. Polyak, K., Haviv, I. & Campbell, I. G. Co-evolution of tumor cells and their microenvironment. *Trends Genet.* **25**, 30–38 (2009).
80. Bottoni, G. et al. CSL controls telomere maintenance and genome stability in human dermal fibroblasts. *Nat. Commun.* **10**, 3884 (2019).
81. Katarkar, A. et al. NOTCH1 gene amplification promotes expansion of cancer associated fibroblast populations in human skin. *Nat. Commun.* **11**, 5126 (2020).
82. Kim, D. E. et al. Convergent roles of ATF3 and CSL in chromatin control of cancer-associated fibroblast activation. *J. Exp. Med.* **214**, 2349–2368 (2017).
83. Restivo, G. et al. IRF6 is a mediator of Notch pro-differentiation and tumour suppressive function in keratinocytes. *EMBO J.* **30**, 4571–4585 (2011).
84. Feric, M. et al. Self-assembly of multi-component mitochondrial nucleoids via phase separation. *EMBO J.* **40**, e107165 (2021).
85. Shevchenko, A., Tomas, H., Havli, J., Olsen, J. V. & Mann, M. In-gel digestion for mass spectrometric characterization of proteins and proteomes. *Nat. Protoc.* **1**, 2856–2860 (2006).
86. Käll, L., Storey, J. D., MacCoss, M. J. & Noble, W. S. Assigning significance to peptides identified by tandem mass spectrometry using decoy databases. *J. Proteome Res.* **7**, 29–34 (2008).
87. Nesvizhskii, A. I., Keller, A., Kolker, E. & Aebersold, R. A statistical model for identifying proteins by tandem mass spectrometry. *Anal. Chem.* **75**, 4646–4658 (2003).
88. Martin-Campos, T. et al. MsViz: a graphical software tool for in-depth manual validation and quantitation of post-translational modifications. *J. Proteome Res.* **16**, 3092–3101 (2017).
89. Perez-Riverol, Y. et al. The PRIDE database resources in 2022: a hub for mass spectrometry-based proteomics evidences. *Nucleic Acids Res.* **50**, D543–D552 (2022).
90. Li, H. & Durbin, R. Fast and accurate short read alignment with Burrows-Wheeler transform. *Bioinformatics* **25**, 1754–1760 (2009).
91. Zhang, Y. et al. Model-based analysis of ChIP-Seq (MACS). *Genome Biol.* **9**, R137 (2008).
92. Heinz, S. et al. Simple combinations of lineage-determining transcription factors prime cis-regulatory elements required for macrophage and B cell identities. *Mol. Cell* **38**, 576–589 (2010).
93. Buenrostro, J. D., Wu, B., Chang, H. Y. & Greenleaf, W. J. ATAC-seq: a method for assaying chromatin accessibility genome-wide. *Curr. Protoc. Mol. Biol.* **109**, 21 29 1–21 29 9 (2015).
94. Buenrostro, J. D., Giresi, P. G., Zaba, L. C., Chang, H. Y. & Greenleaf, W. J. Transposition of native chromatin for fast and sensitive epigenomic profiling of open chromatin, DNA-

- binding proteins and nucleosome position. *Nat. Methods* **10**, 1213–1218 (2013).
95. Corces, M. R. et al. An improved ATAC-seq protocol reduces background and enables interrogation of frozen tissues. *Nat. Methods* **14**, 959–962 (2017).
96. Yu, G., Wang, L. G. & He, Q. Y. ChIPseeker: an R/Bioconductor package for ChIP peak annotation, comparison and visualization. *Bioinformatics* **31**, 2382–2383 (2015).
97. Louault, K., Li, R.-R. & DeClerck, Y. A. Cancer-associated fibroblasts: understanding their heterogeneity. *Cancers* **12**, 3108 (2020).

Acknowledgements

We thank Dr. An Buckinx for critical reading and help with the manuscript, Tatiana Proust for technical assistance, Francesca Guana and Markus Kirolos Youssef for bioinformatic analysis, Anastasia Samarkina and other members of the laboratory for insightful discussions and suggestions. The Central Imaging Facility (CIF), the Electron Microscopy Facility (EMF) and the Protein Analysis Facility (PAF) of the University of Lausanne are gratefully acknowledged for their services and support. This study was supported by grants from the Swiss National Science Foundation (310030B_176404 “Genomic instability and evolution in cancer stromal cells”) and the NIH (R01AR039190, R01AR078374, R01CA269356, the contents do not necessarily represent the official views of the NIH). J.I. has been supported by the European Union’s Horizon 2020 Research and Innovation Program under Marie Skłodowska-Curie Grant Agreement No 859860. G.P.D. is a member of the SKINTEGRITY.CH collaborative research program.

Author contributions

S.G., J.I., P.O., L.M., A.T., M.D., J.R.W. and C.S. performed experiments and/or analyzed the results with G.P.D. S.G. and G.P.D. designed the study and wrote the manuscript.

Competing interests

The authors declare no competing interests.

Additional information

Supplementary information The online version contains supplementary material available at <https://doi.org/10.1038/s41467-024-52344-z>.

Correspondence and requests for materials should be addressed to Soumitra Ghosh or G. Paolo Dotto.

Peer review information *Nature Communications* thanks the anonymous reviewers for their contribution to the peer review of this work. A peer review file is available.

Reprints and permissions information is available at <http://www.nature.com/reprints>

Publisher’s note Springer Nature remains neutral with regard to jurisdictional claims in published maps and institutional affiliations.

Open Access This article is licensed under a Creative Commons Attribution-NonCommercial-NoDerivatives 4.0 International License, which permits any non-commercial use, sharing, distribution and reproduction in any medium or format, as long as you give appropriate credit to the original author(s) and the source, provide a link to the Creative Commons licence, and indicate if you modified the licensed material. You do not have permission under this licence to share adapted material derived from this article or parts of it. The images or other third party material in this article are included in the article’s Creative Commons licence, unless indicated otherwise in a credit line to the material. If material is not included in the article’s Creative Commons licence and your intended use is not permitted by statutory regulation or exceeds the permitted use, you will need to obtain permission directly from the copyright holder. To view a copy of this licence, visit <http://creativecommons.org/licenses/by-nc-nd/4.0/>.

© The Author(s) 2024